

1 **Conserved and divergent features of DNA methylation in embryonic stem cell-derived**
2 **neurons**

3

4 Sally Martin^{1*}, Daniel Poppe^{2,3*}, Nelly Olova^{4,7}, Conor O'Leary⁵, Elena Ivanova⁴, Jahnvi
5 Pflueger^{2,3}, Jennifer Dechka¹, Rebecca K. Simmons^{2,3}, Helen M. Cooper⁵, Wolf Reik^{4,6}, Ryan
6 Lister^{2,3,#}, Ernst J. Wolvetang^{1,#}

7

8 ¹Australian Institute for Bioengineering and Nanotechnology, The University of Queensland,
9 Brisbane, QLD 4072, Australia.

10 ²Australian Research Council Centre of Excellence in Plant Energy Biology, School of
11 Molecular Sciences, The University of Western Australia, Perth, WA 6009, Australia

12 ³The Harry Perkins Institute of Medical Research, Perth, WA 6009, Australia.

13 ⁴Epigenetics ISP, The Babraham Institute, Cambridge, CB22 3AT, UK.

14 ⁵Queensland Brain Institute, The University of Queensland, Brisbane, QLD 4072, Australia.

15 ⁶ The Wellcome Trust Sanger Institute, Hinxton, CB10 1SA, UK.

16 ⁷current address: MRC Institute of Genetics and Molecular Medicine, The University of
17 Edinburgh, Edinburgh, EH4 2XU, UK.

18 * These authors contributed equally

19 # Corresponding authors:

20 • Ernst J. Wolvetang (e.wolvetang@uq.edu.au) Tel +61 7 3346 3894, Fax: +61 7
21 3346 3973, Australian Institute for Bioengineering and Nanotechnology, The
22 University of Queensland, Brisbane, QLD 4072, Australia.

23 • Ryan Lister (ryan.lister@uwa.edu.au) Tel +61 8 6488 4407, ARC Center of
24 Excellence in Plant Energy Biology, The University of Western Australia, and The
25 Harry Perkins Institute of Medical Research, Perth, WA 6009, Australia.

26

27 **Abstract**

28 DNA methylation functions in genome regulation and is implicated in neuronal maturation.
29 Early post-natal accumulation of atypical non-CG methylation (mCH) occurs in neurons of
30 mice and humans, but its precise function remains unknown. Here we investigate mCH
31 deposition in neurons derived from mouse ES-cells *in vitro* and in cultured primary mouse
32 neurons. We find that both acquire comparable levels of mCH over a similar period as *in vivo*.
33 *In vitro* mCH deposition occurs concurrently with a transient increase in *Dnmt3a* expression,
34 is preceded by expression of the post-mitotic neuronal marker *Rbfox3* (NeuN) and is enriched
35 at the nuclear lamina. Despite these similarities, whole genome bisulfite sequencing reveals
36 that mCH patterning in mESC-derived neurons partially differs from *in vivo*. mESC-derived
37 neurons therefore represent a valuable model system for analyzing the mechanisms and
38 functional consequences of correct and aberrantly deposited CG and non-CG methylation in
39 neuronal maturation.

40 **Introduction**

41 The unique epigenomic landscape of neurons is hypothesized to allow these post-
42 mitotic cells to respond to diverse environmental stimuli during development and to modify
43 gene transcription in response to activity, while retaining their cellular identity (Cortes-
44 Mendoza et al., 2013, Day et al., 2013, Feng et al., 2010, Graff et al., 2012, Miller and Sweatt,

45 2007, Stroud et al., 2017). DNA methylation is thought to play an important role in imparting
46 this simultaneous robustness and adaptability to neurons (Bayraktar and Kreutz, 2018b,
47 Bayraktar and Kreutz, 2018a, Fasolino and Zhou, 2017). In most somatic cells, DNA
48 methylation is largely restricted to cytosines in the context of CG dinucleotides (mCG). The
49 methylation of CG sites is considered a relatively stable modification with a well-described
50 function in gene silencing and imprinting (Bird, 2002). In contrast, in adult mammalian brains,
51 other types of DNA methylation are found at high levels, including non-CG methylation (mCH,
52 where H = A, T, or C (Guo et al., 2014, He and Ecker, 2015, Lister et al., 2013, Xie et al.,
53 2012) and intermediates in the DNA demethylation pathway, particularly 5-
54 hydroxymethylcytosine (5hmC) (Kriaucionis and Heintz, 2009, Lister et al., 2013, Mellen et al.,
55 2012, Szulwach et al., 2011). In adult human and mouse neurons up to ~50% of methylated
56 cytosines in the genome occur in the mCH context, a level similar to mCG (Guo et al., 2014,
57 Lister et al., 2013), and the majority of this exists in the mCA sequence context. While the
58 precise roles of these modifications are not fully understood, the complex and diverse
59 methylation profiles of adult neurons (Luo et al., 2017) suggest that DNA methylation plays an
60 important role in the dynamic and adaptable regulation of gene expression in these cells.
61 Studies in both mice and humans have shown that mCA is first observed in the brain shortly
62 after birth and continues to accumulate during development to adulthood, after which the
63 levels remain stable (Lister et al., 2013). This observation raises the exciting possibility that
64 the generation of mCA may link early life experiences with neuron function later in life. The
65 level of intragenic mCA in neurons inversely correlates with transcript abundance (Mo et al.,
66 2015, Stroud et al., 2017, Xie et al., 2012), and in mice mCA deposition is negatively regulated
67 by gene transcription (Stroud et al., 2017), suggesting that mCA functions as a part of a
68 molecular system to modulate gene expression in response to synaptic activity, and to
69 consolidate specificity of neuron subtypes.

70 DNA methylation is established and maintained by a family of conserved DNA
71 (cytosine-5)-methyltransferases (DNMTs). Dnmt1 propagates existing methylation patterns at

72 symmetrically opposed CG sites during cell division and is essential for the maintenance of
73 methylation and chromosomal stability (Bayraktar and Kreutz, 2018a, Feng and Fan, 2009).
74 Dnmt3a and Dnmt3b, on the other hand, catalyse the *de novo* methylation of cytosine, and
75 the levels of Dnmt3a can be dynamically regulated to increase DNA methylation in the brain
76 (Feng et al., 2005). The post-natal deposition of mCH is driven by a transient increase in the
77 expression of Dnmt3a (Gabel et al., 2015, Guo et al., 2014, Lister et al., 2013, Luo et al., 2019,
78 Stroud et al., 2017), and conditional deletion of Dnmt3a in Nestin-positive neuronal precursors
79 during late gestation results in impaired motor activity (Nguyen et al., 2007). In contrast,
80 deletion of Dnmt3a in excitatory neurons at early postnatal stages was reported to have no
81 apparent major effect on brain development or function (Feng et al., 2010), suggesting that
82 the developmental window during which mCH is deposited is critical (Lister et al., 2013). The
83 importance of DNA methylation in governing correct neuronal function is exemplified by a
84 range of developmental neurological disorders that result from mutations in proteins
85 associated with DNA methylation in both the CG and CH context (Hamidi et al., 2015, Ip et al.,
86 2018).

87 Defining the roles of mCG and mCH in neuron maturation and synaptic plasticity is of
88 fundamental importance for understanding normal and abnormal brain development, thus a
89 tractable and representative *in vitro* model system to further explore this process is highly
90 desirable. We therefore investigated the levels, distribution and temporal dynamics of mCH
91 during *in vitro* neuronal differentiation of human and mouse pluripotent stem cells. Deploying
92 a range of cellular and genomic assays, we reveal similar sub-nuclear patterning, levels, and
93 spatiotemporal dynamics of DNA methylome reconfiguration during the differentiation and
94 maturation of mouse neurons *in vitro* and *in vivo*, but also differences that likely arise from the
95 complex influence of the *in vivo* cellular environment on neuron differentiation and maturity.

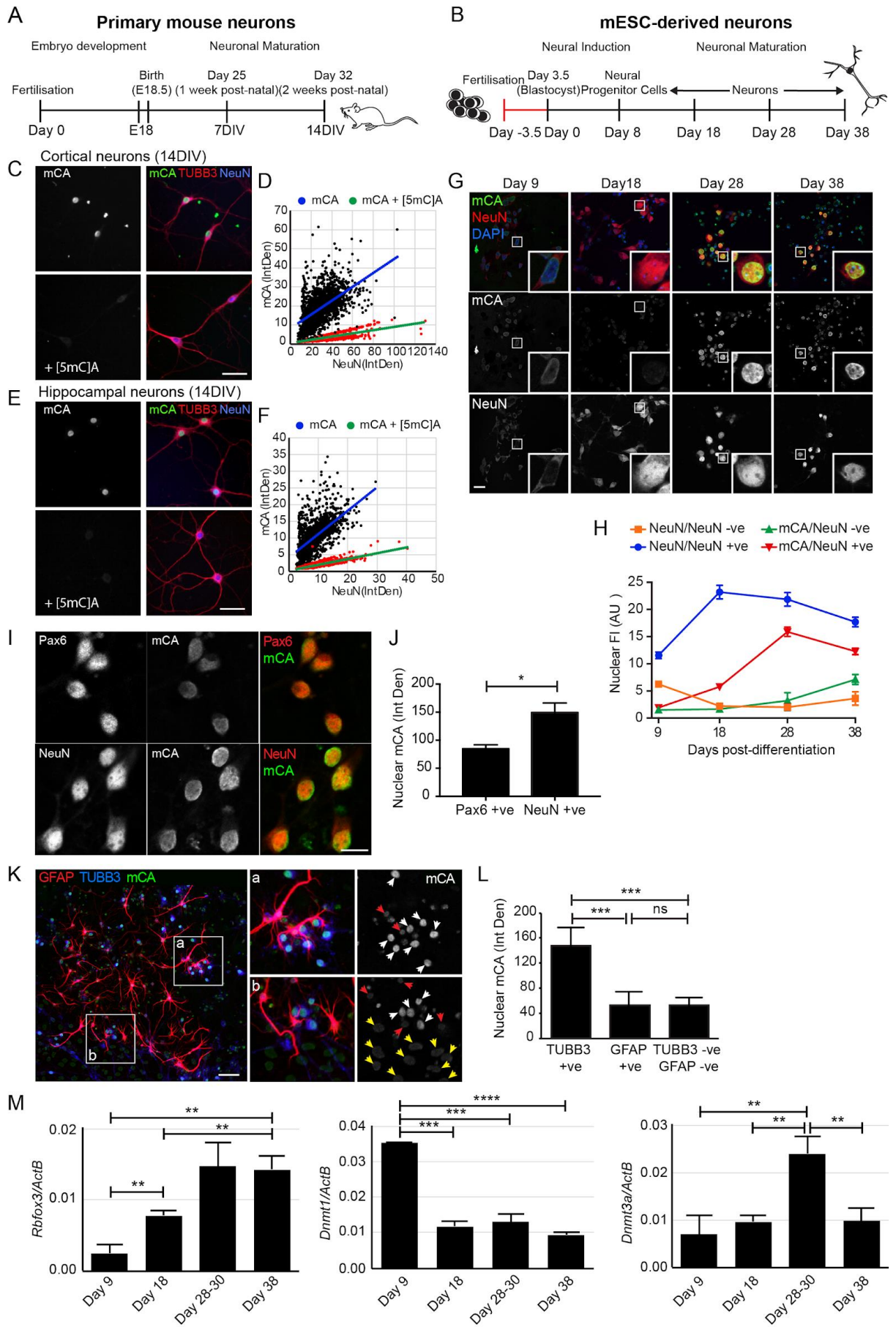
96

97 **Results**

98 **Immunocytochemical labelling for mCA accumulates in post-mitotic neurons and**
99 **temporally correlates with DNMT3a expression.**

100 *In vivo*, mouse cortical neurons begin to acquire readily detectable levels of mCH around 2
101 weeks after birth, which continues to increase up to 6 weeks of age and remains high
102 throughout adulthood (Lister et al., 2013). To assess whether this can be recapitulated *in vitro*,
103 we used two independent approaches. First, we isolated primary cortical and hippocampal
104 neurons from day 18 embryonic C57BL/6 mice (E18, average gestation 18.5 days) and
105 cultured these for up to 14 days *in vitro* (DIV). We hypothesized that if mCH accumulation was
106 due to cell intrinsic developmentally hardwired processes, 14DIV should correlate with the
107 temporal acquisition of mCH *in vivo* (Figure 1A). In the second approach, we adapted an
108 established differentiation protocol to generate mouse cortical neurons from embryonic stem
109 cells (mESCs) (Bibel et al., 2007). We hypothesized that if this developmental model
110 recapitulated neural development and neuronal maturation *in vivo*, mCH would occur within
111 several weeks (Figure 1B). Two different mouse ESC lines, R1 (Nagy et al., 1993) and G4
112 (George et al., 2007), were differentiated as cell aggregates for 8 days in suspension, followed
113 by dissociation and continued differentiation in adherent culture for up to 30 additional days to
114 yield mixed cultures enriched in post-mitotic neurons (Supplementary Figure 1A). Both cell
115 lines developed mature neurons within an equivalent time course and to a similar extent, as
116 assessed by morphology and immunohistochemistry (R1 and G4), TEM analysis of synaptic
117 depolarization (R1), and c-Fos mRNA and ICC analysis following depolarization (G4)
118 (Supplementary Figure 1). To investigate the temporal acquisition, sub-nuclear localisation,
119 and cell-type specificity of mCH in cultured neurons, we used an antibody raised against the
120 mCA dinucleotide (anti-mCA) to analyse the primary- and mESC-derived neuronal cultures by
121 immunocytochemistry. To identify neurons, cultures were co-labelled for NeuN/Rbfox3, a well-
122 established marker of most postmitotic neuron subtypes, and beta3-tubulin (TUBB3), a pan-
123 neuronal marker. Specificity of the mCA antibody was confirmed using a panel of competitive
124 methylated oligonucleotides (Figure 1C – 1F, Supplementary Figure 2).

Martin et al., Figure 1



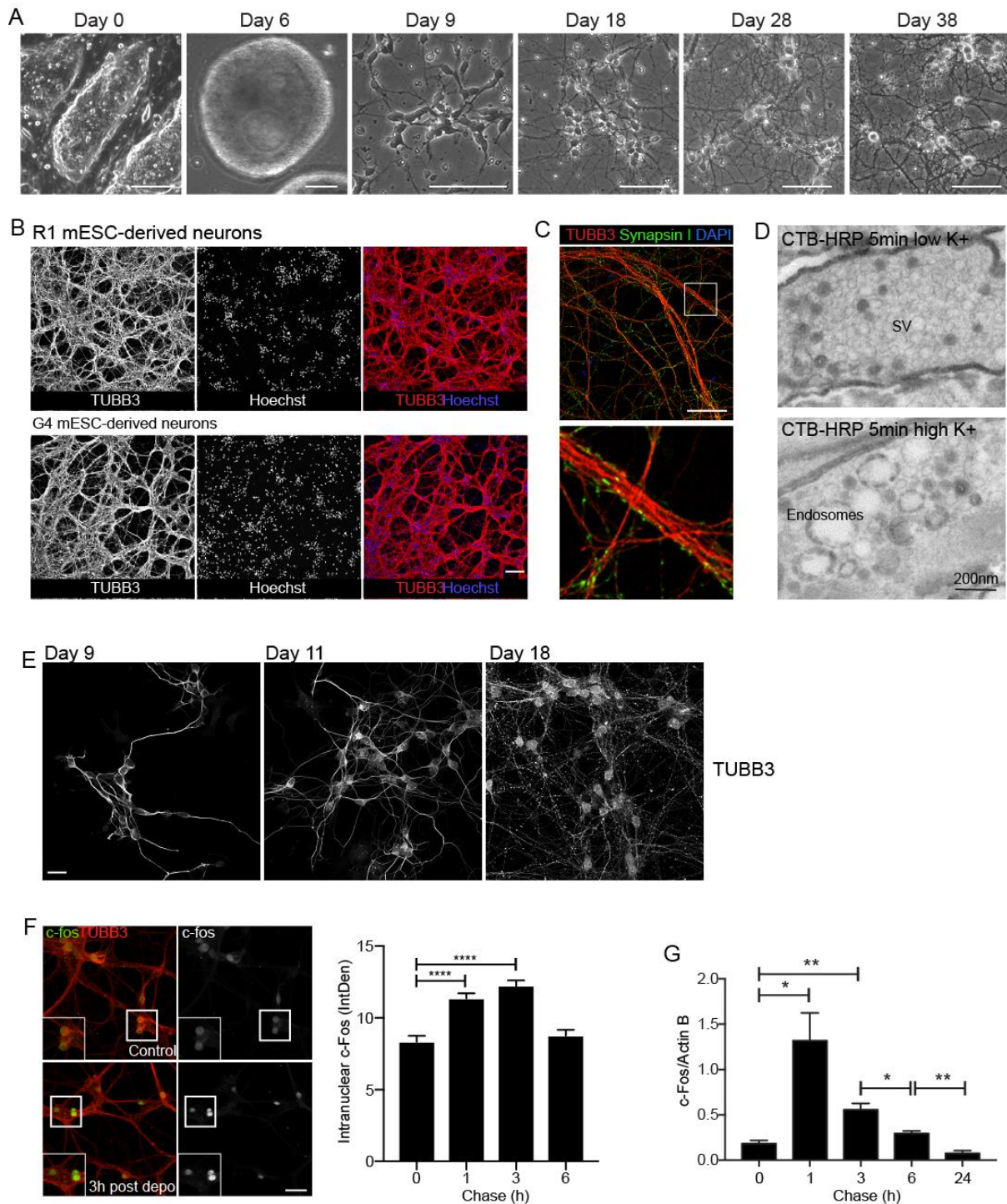
126 **Figure 1 In vitro acquisition of DNA methylation in primary and ESC-derived mouse**
127 **neurons**

128 **(A, B)** Timeline schematic of neuron development in mouse cortex (A) and from mESCs in
129 vitro (B). **(C-F)** 14DIV cortical (C, D) or hippocampal (E, F) neurons immunolabelled for NeuN,
130 TUBB3 and mCA $\pm 2.5 \mu\text{M}$ [5mC]A. Scale bar = 50 μm . Analysis of the relative intensity of
131 NeuN and mCA fluorescence in DAPI-masked nuclei from 14DIV cortical (D) or hippocampal
132 (F) neurons. **(G, H)** mESC-derived neurons were fixed at different times during maturation and
133 labelled for NeuN, mCA and DAPI. Scale bar = 20 μm . The nuclear fluorescence intensity (AU)
134 of NeuN and mCA was determined. Results = mean \pm SEM, for one representative
135 differentiation. Similar labelling profiles were observed in 3 separate differentiations. **(I, J)**
136 Neural progenitors (Day 9-10, Pax6+ve) and neurons (Day 20-40 NeuN+ve) were
137 immunolabeled for mCA, and level of mCA nuclear fluorescence intensity quantified. Results
138 = mean \pm SD, n=3 separate differentiations for Pax6 and 2 differentiations for NeuN. Scale
139 bar = 10 μm . **(K, L)** Later stage neural differentiations (Day 30-38) were immunolabeled for
140 astrocytes (GFAP), neurons (TUBB3) and mCA. Nuclei were manually masked and the level
141 of mCA measured in TUBB3+ve neuronal cells, GFAP+ve astrocytes, and GFAP-ve/TUBB3-
142 ve cells of unknown identity. Quantitation shown was acquired from a single late-stage
143 differentiation and labelling averaged across 5 random fields of view. Results are the mean \pm
144 SD. Arrows mark nuclei of astrocytes (red), neurons (white), and other cell types (yellow).
145 Scale bar = 50 μm . **(M)** Gene expression of *Dnmt1*, *Dnmt3a* and *Rbfox3* (NeuN) were
146 determined by RT-qPCR relative to beta-actin. Results = mean \pm SEM, n=3-4. For all
147 experiments, statistical analysis was performed using a Student's t-test. * $p < 0.01$, ** $p < 0.05$,
148 *** $p < 0.001$, **** $p < 0.0001$.

149

150

Martin et al. Supplementary Figure 1



151

152 **Supplementary Figure 1 Characterisation of mESC-derived neurons**

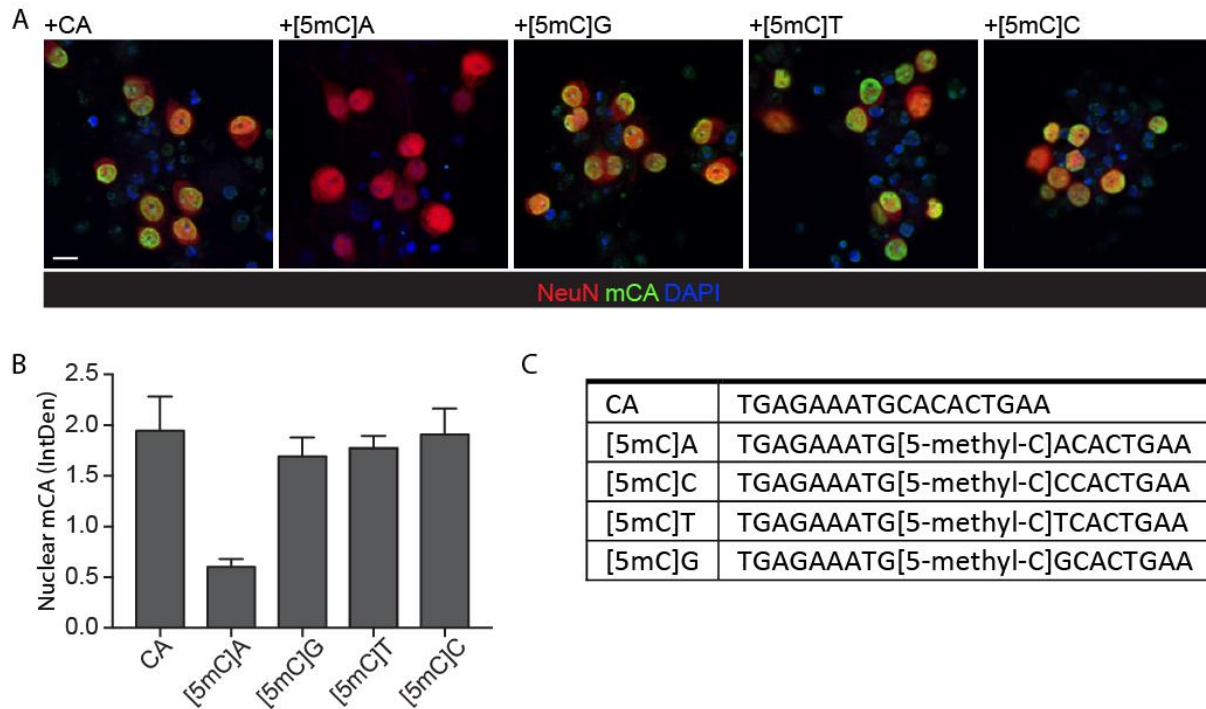
153 **(A)** Phase contrast images of mESCs growing on a layer of feeder MEFs, cell aggregates (day
154 6), neural progenitors (day 9), and neurons (day 18-38). Scale bar =100 μm, except for cell

155 aggregates = 200 μm . **(B)** Neurons derived from either G4 mESCs or R1 mESCs were fixed
156 and labelled for the pan-neuronal marker beta3-tubulin (TUBB3). Both cell lines generated
157 complex neurite networks within 38 days. Scale bar = 100 μm . **(C)** Neurons derived from G4
158 mESCs were fixed and labelled for TUBB3 and the pre-synaptic protein synapsin 1. Punctate
159 labelling for Syn1 along neurites demonstrates the presence of nascent synapses. Scale bar
160 = 50 μm . **(D)** The response of synapses to depolarisation was shown by transmission electron
161 microscopy. R1 mESC-derived neurons were incubated for 5 min in the presence of CTB-HRP
162 in either low K^+ or high K^+ buffer. Low levels of tracer endocytosis into synaptic vesicles in low
163 K^+ was superseded by high levels of bulk endocytosis in depolarised cells, suggesting a strong
164 rapid burst of neuroexocytosis and compensatory endocytosis (Cousin, 2009). **(E)** G4 mESC-
165 derived neurons were fixed and labelled for TUBB3 at different time points during
166 differentiation. Scale bar = 20 μm . **(F)** G4 mESC-derived neurons were depolarised for 5 min
167 with high K^+ , then chased in growth medium for between 1h and 6 h. Cells were fixed and
168 labelled for c-Fos and TUBB3. The intranuclear intensity (IntDen) of c-Fos was determined
169 during the chase. Results = mean \pm SEM, for one representative differentiation. Similar
170 labelling profiles were observed in two separate differentiations. Depolarisation resulted in a
171 transient increase in intranuclear c-Fos labelling in the post-depolarisation period. **** p
172 <0.0001 , Student's t -test. Scale bar = 50 μm . **(G)** c-Fos mRNA abundance was determined by
173 RT-qPCR in control G4 mESC-derived neurons and during a 24 h chase following a 5 min
174 transient depolarisation by high K^+ . Results shown are mean \pm SEM relative to beta-actin
175 levels. $N=3$ independent experiments. * $p <0.05$, ** $p <0.01$, Student's t -test.

176

177

Martin et al. Supplementary Figure 2



178

179 **Supplementary Figure 2 Specificity of the anti-mCA antibody determined by ICC**

180 **(A)** mESC-derived neurons were fixed and immunolabelled for NeuN and mCA \pm 2.5 μ M
 181 competitive methylated oligonucleotides: [5mC]A, [5mC]G, [5mC]T and [5mC]C, or the non-
 182 methylated CA oligonucleotide. Scale bar = 10 μ m. **(B)** The Integrated Density (IntDen) of the
 183 nuclear mCA labelling in NeuN-masked nuclei was determined. **(C)** Sequence of the
 184 methylated oligonucleotides.

185

186 To first determine whether *in vitro* cultured neurons could acquire non-CG methylation, 14DIV
 187 cortical and hippocampal primary neuronal cultures were immunolabelled for mCA, NeuN, and
 188 TUBB3 (Figure 1C, E). At this DIV, the majority of cells displayed a strong intranuclear labelling
 189 for mCA, in addition to labelling for both neuronal markers. Nuclear labeling for mCA was
 190 completely abrogated by the competitive [5mC]A oligonucleotide (Figure 1C-F,
 191 Supplementary Figure 2) confirming the specificity of the antibody. To quantify mCA labelling,

192 cell nuclei were masked using DAPI fluorescence and the level of mCA and NeuN
193 immunofluorescence in individual nuclei measured. The relative levels of mCA to NeuN were
194 then determined (Figure 1D, 1F). Consistent with the enrichment of mCA in neurons, we found
195 a strong positive correlation between the level of NeuN labelling and the level of mCA labelling
196 in both hippocampal ($r=0.62$) and cortical ($r=0.83$) cells.

197 We next used the anti-mCA antibody to analyse the accumulation of mCA at different
198 times up to 38 days during the differentiation and maturation of the mESC-derived neurons
199 (Figure 1G, H). Neuronal cells expressed TUBB3 one day after attachment (day 9,
200 Supplementary Figure 1E), and detectable NeuN labelling was observed within 3-6 days of
201 attachment (differentiation day 11-14, Figure 1G), suggesting the rapid development of a post-
202 mitotic phenotype. Interestingly, this temporally correlates with the initial identification of NeuN
203 at E10.5 in the embryonic mouse brain (Mullen et al., 1992), suggesting that these
204 developmental milestones are temporarily hardwired and can be recapitulated *in vitro*.
205 Consistent with the early development of post-mitotic neurons, there was no further increase
206 in the number of NeuN-positive neurons over the 4 weeks in adherent culture, although there
207 was an obvious but variable increase in the number of non-neuronal cells within this time,
208 including glial cells (see Figure 1K), as described previously (Bibel et al., 2004).
209 Immunocytochemical (ICC)-based analysis of DNA methylation in NeuN-positive cells
210 revealed an increase in the level of nuclear mCA labeling between days 18 and 28, which
211 remained high to day 38 (Figure 1G, H). As the initial observation of mCA was significantly
212 later than the initial observation of NeuN, a post-mitotic phenotype is likely a prerequisite for
213 subsequent acquisition of mCA. Consistent with this, we found only minimal labelling for mCA
214 in Pax6-positive neural progenitors differentiated for 9-10 days relative to ~2-fold higher levels
215 in NeuN-positive neurons differentiated for 28-38 days (Figure 1I, J). Similarly, we found
216 minimal labelling for mCA in GFAP-positive glial cells and in additional unidentified cell types
217 within the cultures that did not label for either neuronal or glial markers (Figure 1K, L).

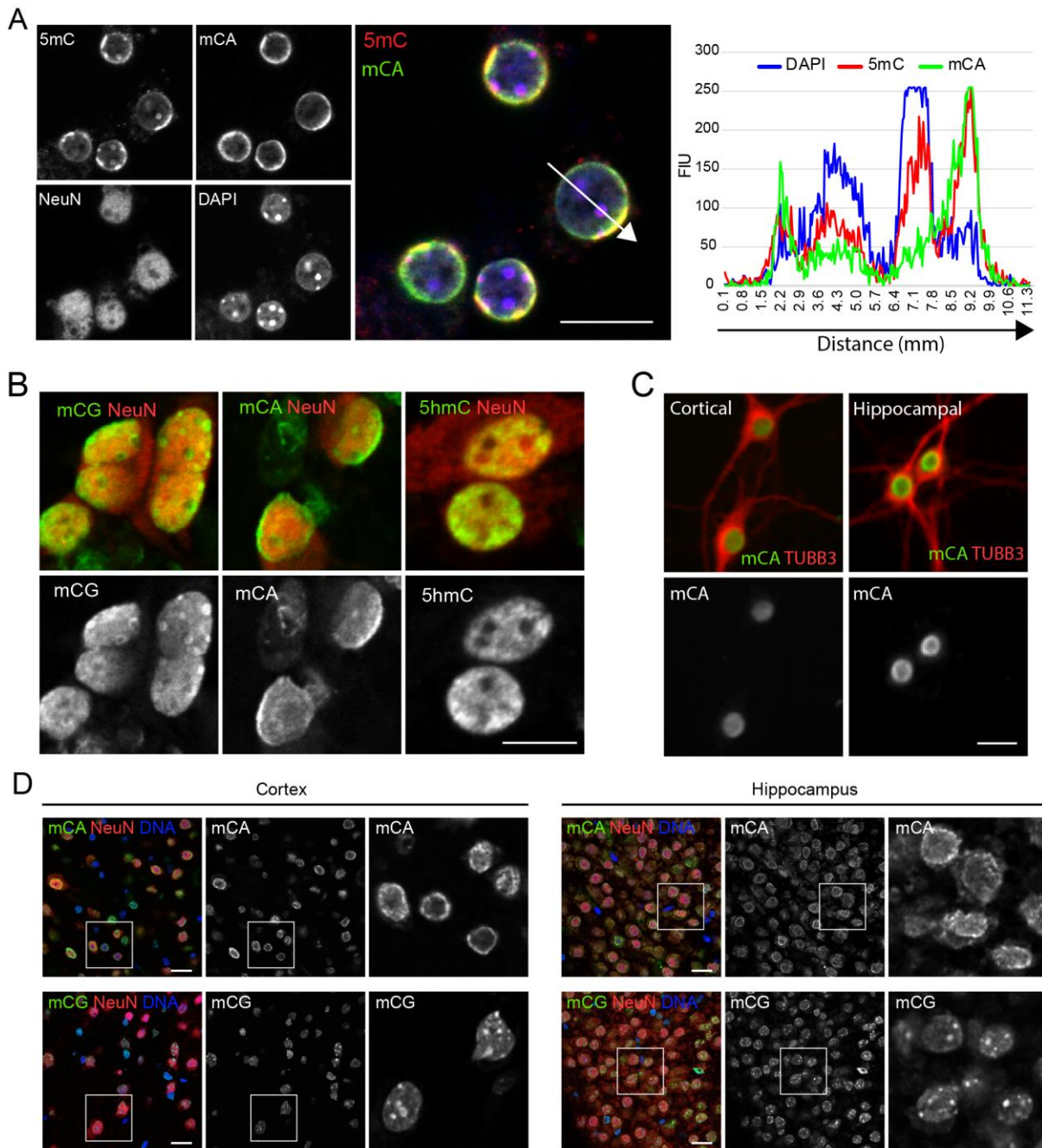
218 Methylation of CH sites has been shown to be catalysed by Dnmt3a *in vivo* (Feng et
219 al., 2005, Stroud et al., 2017). We therefore analysed the transcript abundance of *Rbfox3*
220 (NeuN) and the DNA methyltransferases *Dnmt3a* and *Dnmt1* during differentiation by RT-
221 qPCR (Figure 1M). Consistent with the results of the ICC, *Rbfox3* (NeuN) expression was
222 found to significantly increase between days 9 and 18, reaching a plateau around day 28. In
223 contrast, and in agreement with previous data from both primary neurons and mouse brain
224 (Feng et al., 2005, Lister et al., 2013), *Dnmt3a* expression transiently increased between days
225 18 and 28 of differentiation and decreased again by 38 days. This transient increase in *Dnmt3a*
226 transcript level temporally correlates with the accumulation of mCA labelling observed by ICC
227 in the neurons (Figure 1G), strongly supporting the prediction that *Dnmt3a* catalyses CA
228 methylation in the mESC-derived neurons. *Dnmt1* expression was initially high (Day 9) but
229 rapidly decreased after cell attachment, consistent with a role in the maintenance of DNA
230 methylation in the mitotic neural precursors. Collectively these data demonstrate that mCA
231 deposition occurs specifically in post-mitotic neurons but not in non-neuronal cell types and
232 correlates with DNMT3a expression.

233

234 **mCA associates with the nuclear lamina in neurons**

235 During our ICC analysis of mCA labelling, we observed that this DNA modification was
236 enriched near the nuclear periphery in our *in vitro* neuronal cultures. To determine whether
237 this localisation was unique to mCA, ESC-derived neurons were co-labelled for total 5-
238 methylcytosine (5mC) using an antibody predicted to label both mCG and mCH, and with the
239 mCA-specific antibody, and the intranuclear distribution of the two compared (Figure 2A).

Martin et al., Figure 2



240

241 **Figure 2 Intranuclear localisation of mCA in vivo, in primary mouse neurons and in**

242 **mESC-derived neurons**

243 **(A)** mESC-derived neurons were immunolabelled for total 5mC (mCG + mCH), mCA, and

244 NeuN, and nuclei identified using DAPI. Scale bar = 10µm. **(B)** mESC-derived neurons

245 immunolabelled for NeuN and either mCG, mCA, or 5hmC. Scale bar = 10µm. **(C)** Primary

246 *mouse hippocampal and cortical neurons (14DIV) were labelled for mCA and TUBB3. Scale*
247 *bar = 20µm. (D) Immunohistochemical analysis of DNA methylation in adult mouse*
248 *hippocampus and cortex immunolabeled for either mCG or mCA, and NeuN, and nuclei*
249 *identified using YOYO1. Scale bar = 20 µm.*

250 Consistent with a more restricted intranuclear distribution of mCA, total 5mC labelling was
251 observed to be more broadly distributed within the nucleus. While both marks showed a diffuse
252 labeling, mCA was highly enriched at the nuclear periphery, whereas 5mC additionally strongly
253 labelled intranuclear foci, which were devoid of mCA labelling. The intensely labelled 5mC foci
254 were found to also stain strongly with DAPI (Figure 2A) suggesting regions of tightly packed
255 heterochromatin that exclude mCA methylated DNA, in agreement with previous studies in
256 mouse brain (Lister et al., 2013, Stroud et al., 2017).

257 To directly examine the distribution of DNA methylated in specific sequence contexts,
258 neurons were labelled for either mCA or using an antibody specific for mCG (Figure 2B). In
259 addition, we examined localisation of 5-hydroxymethylcytosine (5hmC) (Figure 2B), which is
260 also highly enriched in neuronal genomic DNA (Kriaucionis and Heintz, 2009, Mellen et al.,
261 2012, Szulwach et al., 2011). This labelling confirmed that the intense DAPI-stained foci
262 observed in Figure 2A were enriched in mCG labelling. Again, mCA was enriched at the
263 nuclear periphery, suggesting an association with the nuclear lamina. 5hmC was diffusely
264 distributed throughout the nucleus, consistent with an enrichment in euchromatin (Chen et al.,
265 2014).

266 To confirm that the distribution of mCA observed *in vitro* faithfully represented the
267 intranuclear localisation *in vivo*, we analysed the localisation of mCA in primary neurons
268 cultured for 14DIV (Figure 2C), and of mCA and mCG in immunohistochemical sections of
269 adult mouse brain (Figure 2D). Both primary neurons and cortical or hippocampal brain
270 sections showed an identical enrichment of mCA labelling at the nuclear periphery.

271 Collectively these data show that DNA methylated in the CA context associates with the
272 nuclear lamina in neurons.

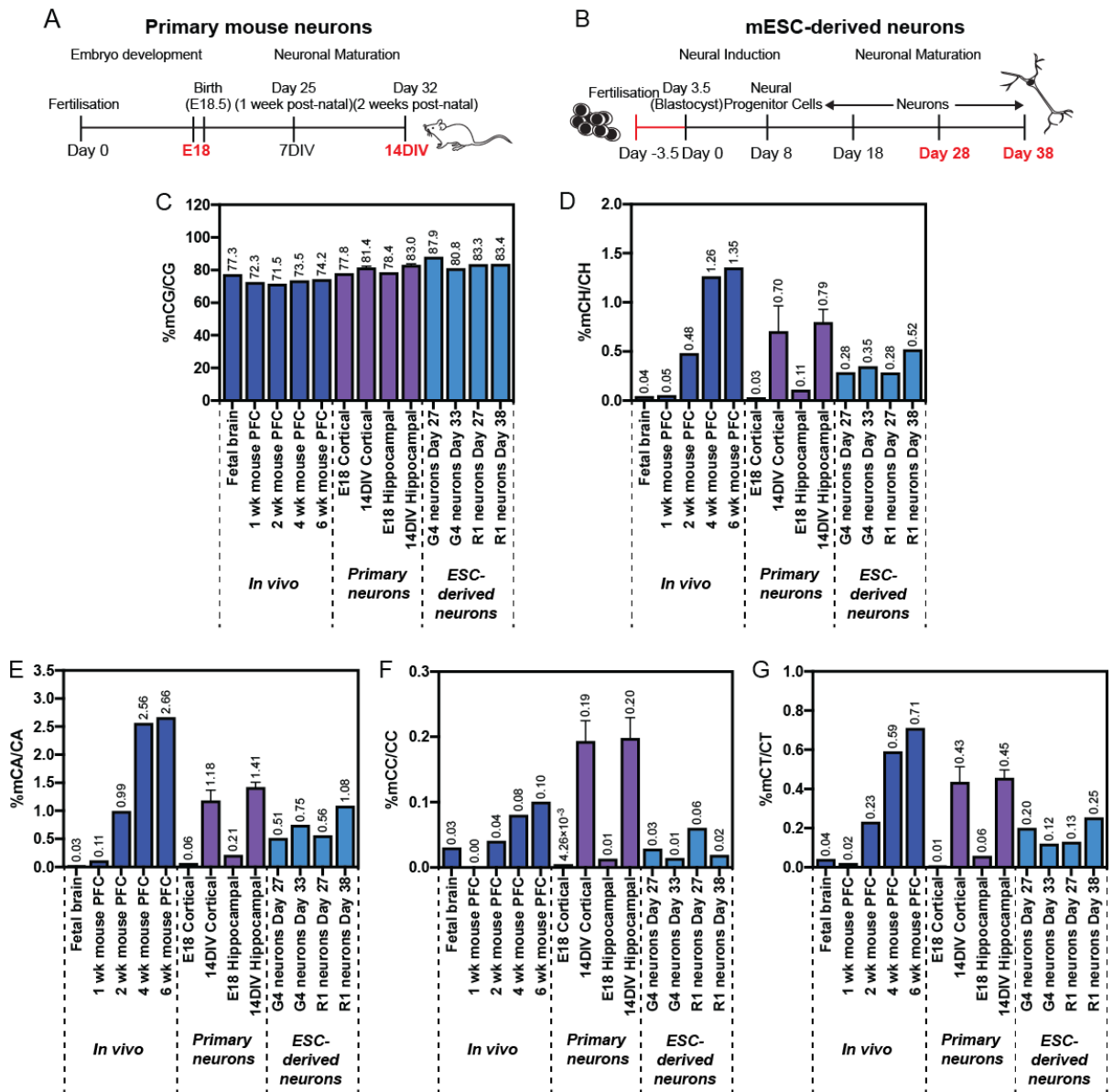
273

274 **mESC-derived neuronal cultures acquire mCH to levels similar to those observed in**
275 **vivo.**

276 Having shown that both mESC-derived neurons and cultured primary neurons
277 acquired mCA labeling using immunocytochemistry, we next determined global levels of DNA
278 methylation (CG and CH) by whole-genome bisulfite sequencing (WGBS).

279 In primary neurons, we found very low levels of mCH (<0.1%) at E18 in cells isolated
280 from either the hippocampus or the cortex, consistent with previous *in vivo* data (Lister et al.,
281 2013) and E12.5 mouse NPCs cultured *in vitro* (Luo et al., 2019). Following 14DIV, this level
282 increased to 0.70% and 0.79% in primary cortical and hippocampal neurons, respectively
283 (Figure 3D), confirming that the mechanisms underpinning accumulation of mCH are
284 conserved in *in vitro* cultures. This is in agreement with the *in vitro* differentiation of E12.5-
285 derived mouse NPCs, which also show an increase in mCH levels over several weeks of
286 culture, reaching a maximum of 0.35% mCH/CH after 21 days (Luo et al., 2019). Analysis of
287 mCH context confirmed that methylation at CA sites was the most abundant modification,
288 although smaller increases in methylation in the CT and CC contexts were also observed
289 (Figure 3E-G). Comparison of the methylation levels at 14DIV to those of 2 week old mouse
290 prefrontal cortex (PFC) (Lister et al., 2013) showed that these were similar for all three mCH
291 subtypes. In contrast, the levels of mCG were slightly higher *in vitro* than *in vivo* (Figure 3C).

Martin et al., Figure 3



292

293

294 **Figure 3 WGBS analysis of DNA methylation in primary mouse neurons and mESC-**

295 **derived neurons**

296 **(A, B)** Timeline schematic of neuron development in mouse cortex (A) and from mESCs in

297 vitro (B). Time points analysed by WGBS are highlighted red. **(C-G)** Global levels of DNA

298 methylation in mouse brain ((Lister et al., 2013), dark blue bars), primary mouse cortical or

299 hippocampal neurons (E18 and 14DIV, purple bars) and mESC-derived neuronal cultures (R1

300 and G4 cell lines, light blue bars). Values represent the weighted methylation levels: the
301 fraction of all WGBS base calls that were C at cytosine positions in the genome (for each
302 context separately). Results = single samples, except 14DIV where $n=2$, mean \pm SD.

303

304 Analysis of global DNA methylation levels by WGBS was then undertaken on the
305 mESC-derived neuronal cultures between days 27 and 38 post-differentiation, which are
306 temporally comparable to approximately 1 week and 3 weeks post-natal *in vivo* development,
307 respectively (Figure 3A, B). Consistent with the primary neuron analysis, both the G4- and R1-
308 derived neuronal cultures acquired high levels of mCH within 27 days, consisting
309 predominantly of mCA. The global level of mCH and mCA was very similar between the two
310 cell lines and showed a time-dependent increase up to 38 days. Global levels of mCA and
311 mCH at 38 days (equivalent to ~3 weeks post-natal *in vivo*) closely mirrored those of the
312 prefrontal cortex of 2 week old mice (Figure 3D, E), although the levels at 27 days (~1 week
313 post-natal *in vivo*) were ~5-fold higher than in 1 week old mouse PFC. Whether this reflects
314 an earlier deposition of mCH *in vitro* or is a result of differing proportions of neuronal and non-
315 neuronal cells in the two sample types is not known. Smaller increases in the level of mCT
316 and mCC were also observed *in vitro*, as well as an increase in the level of mCG. Our data
317 indicate that *in vitro* neuronal differentiation of mESCs recapitulates overall *in vivo* levels of
318 mCH and mCA, which is distinct from prior report of low levels of mCH and mCA in iN cells
319 (Luo et al., 2019). Thus, we conclude that acquisition of mCH and mCA is largely a neuro-
320 developmentally hardwired process.

321

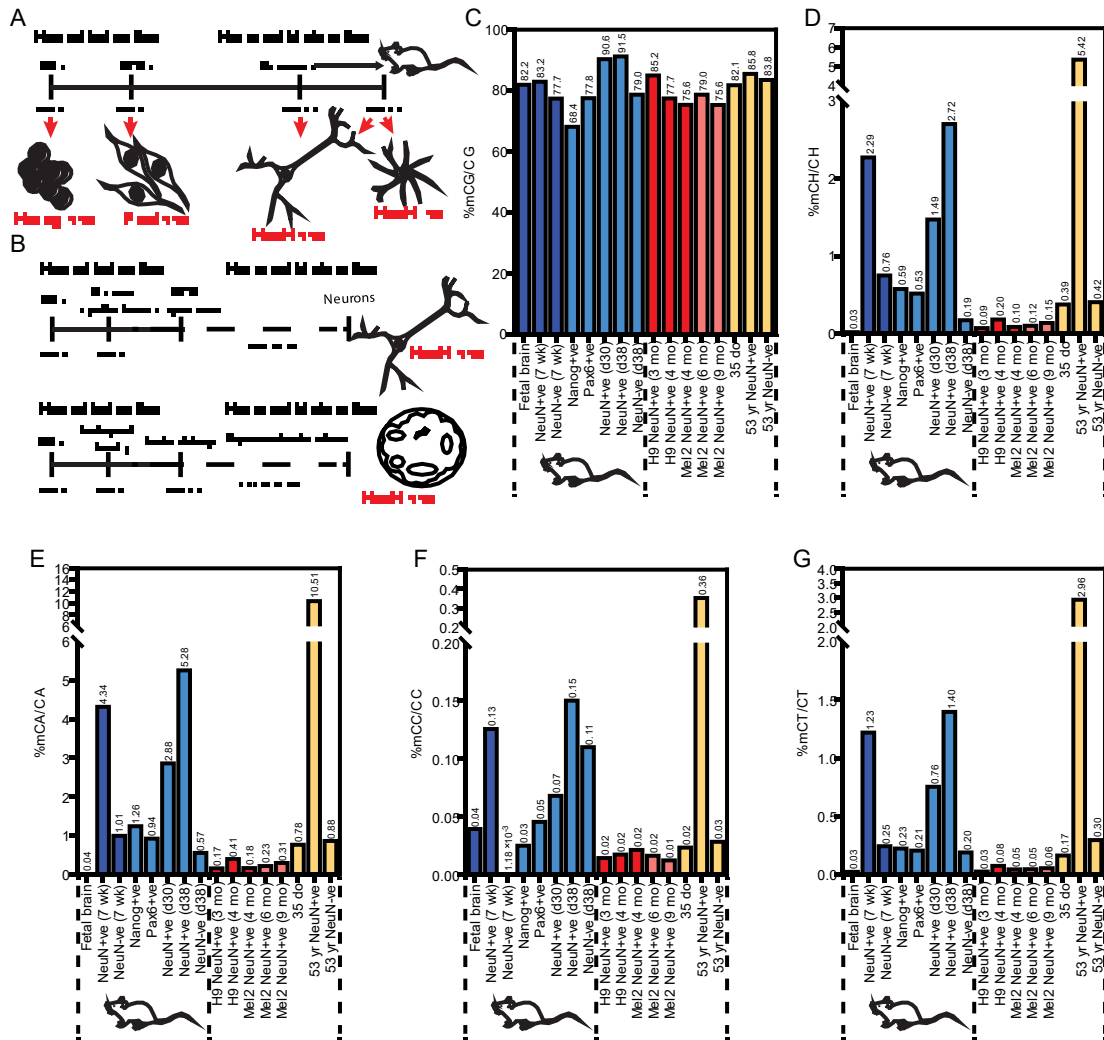
322 **Global mCH and mCG levels in mESC-derived neurons reveals hypermethylation**
323 **relative to *in vivo* adult neurons.**

324 As mESC-derived neuronal cultures contain multiple cell types (Figure 1) fluorescence-
325 activated nuclear sorting (FANS) was used to analyse mCG and mCH levels in specific
326 populations of cells (Figure 4A, B). To analyse the developmental timeline of mESC-derived
327 neurons we sorted Nanog-positive nuclei from mESCs, Pax6-positive nuclei from mESC-
328 derived neuronal progenitor cells, NeuN-positive nuclei from cells cultured for 30 days, and
329 NeuN-positive and NeuN-negative nuclei from cells cultured for 38 days (Figure 4A, see also
330 Figure 1A, B). To investigate a possible temporal regulation of methylation patterns we also
331 isolated NeuN-positive cells from various human ESC-derived neuronal cultures, including
332 both 2-D cortical differentiation (Reinhardt et al., 2013) and 3-D cerebral organoids (Lancaster
333 and Knoblich, 2014) (Figure 4B). We then analysed by WGBS the levels of mCG and mCH in
334 these different nuclear populations, representing different cell types within the various
335 neuronal differentiation timelines (Figure 4A and 4B).

336 During the mouse ESC differentiation process, global CG methylation levels were
337 observed to progressively increase, with the highest increment observed during the maturation
338 of Pax6-positive neural progenitors to 30-day old neuronal nuclei, corresponding to the period
339 during which maximal *Dnmt3a* transcript abundance was observed in bulk cultures (Figure
340 1M). The observed levels of mCG in NeuN-positive nuclei, at both 30 days and 38 days, was
341 substantially higher than that reported in NeuN-positive nuclei isolated from mouse PFC, and
342 was higher than the equivalent NeuN-negative cells in the cultures, suggesting specific
343 hypermethylation of neuronal CG occurs *in vitro*. Interestingly, hypermethylation of CG was
344 not observed in the human cultures, where we observed generally lower global levels of mCG
345 than *in vivo* (for four out of five cultures).

346

Martin et al., Figure 4



347

348 **Figure 4 DNA methylation levels in fluorescence-activated sorted nuclei**

349 **(A, B)** Schematics showing time points during the mESC and hESC differentiation to neurons
 350 at which nuclei were isolated. **(A)** Samples from the mESC differentiation included Nanog +ve
 351 mESCs, Pax6 +ve neural progenitors, day 30 and 38 NeuN +ve mouse neurons and day 38
 352 NeuN -ve cells. **(B)** In the human ESC differentiation, NeuN +ve nuclei were isolated following
 353 12-16 weeks of 2-D culture, or 6-9months of 3-D culture. **(C-G)** Level of DNA methylation in
 354 isolated nuclear populations. Light blue (mouse), red (human 2-D) and pink (human 3-D) bars
 355 show samples generated in this study. Dark blue (mouse) and yellow (human) bars show
 356 previously published levels of DNA methylation (Lister et al., 2013).

357

358 We next analysed the levels of mCH in the various nuclei populations. In the mouse samples,
359 the level of mCH was found to increase substantially during the transition from Pax6-positive
360 NPCs to 30 day old NeuN-positive neurons, and again between day 30 and day 38 of neuron
361 maturation (Figure 4D). The levels attained by day 38 of culture exceeded that of 7 week old
362 mouse prefrontal cortex (approximately 65 days total development from the blastocyst stage),
363 suggesting that for mCH, as for mCG, hypermethylation of the *in vitro*-derived neurons was
364 occurring. This pattern of methylation was recapitulated for the individual analyses of mCA,
365 mCC and mCT (Figure 4E-F). For mCA, we found a level of 1.25% (mCA/CA) in Nanog-
366 positive mESC-derived nuclei, consistent with published studies in mice (Arand et al., 2012,
367 Ramsahoye et al., 2000) and humans (Liao et al., 2015, Ziller et al., 2011). This level was
368 found to decrease in Pax6-positive neural progenitors, and subsequently increased to 2.9%
369 (day 30) and 5.3% (day 38) in NeuN-positive nuclei. As with mCG and mCH, at day 38 this
370 level was higher than that reported in NeuN-positive nuclei isolated from mouse brain, again
371 suggesting hypermethylation of CA. Consistent with the ICC results and published *in vivo* data
372 (Lister et al., 2013), NeuN-negative cells within the 38-day old neuronal cultures contained low
373 levels of mCA. The levels of mCT in the day 38 ESC-derived neurons reached levels similar
374 to those in the adult mouse brain, while only negligible levels of mCC were detected in any
375 cell type. Together these data demonstrate that mESC-derived neurons acquire non-CG
376 methylation levels similar to *in vivo* levels.

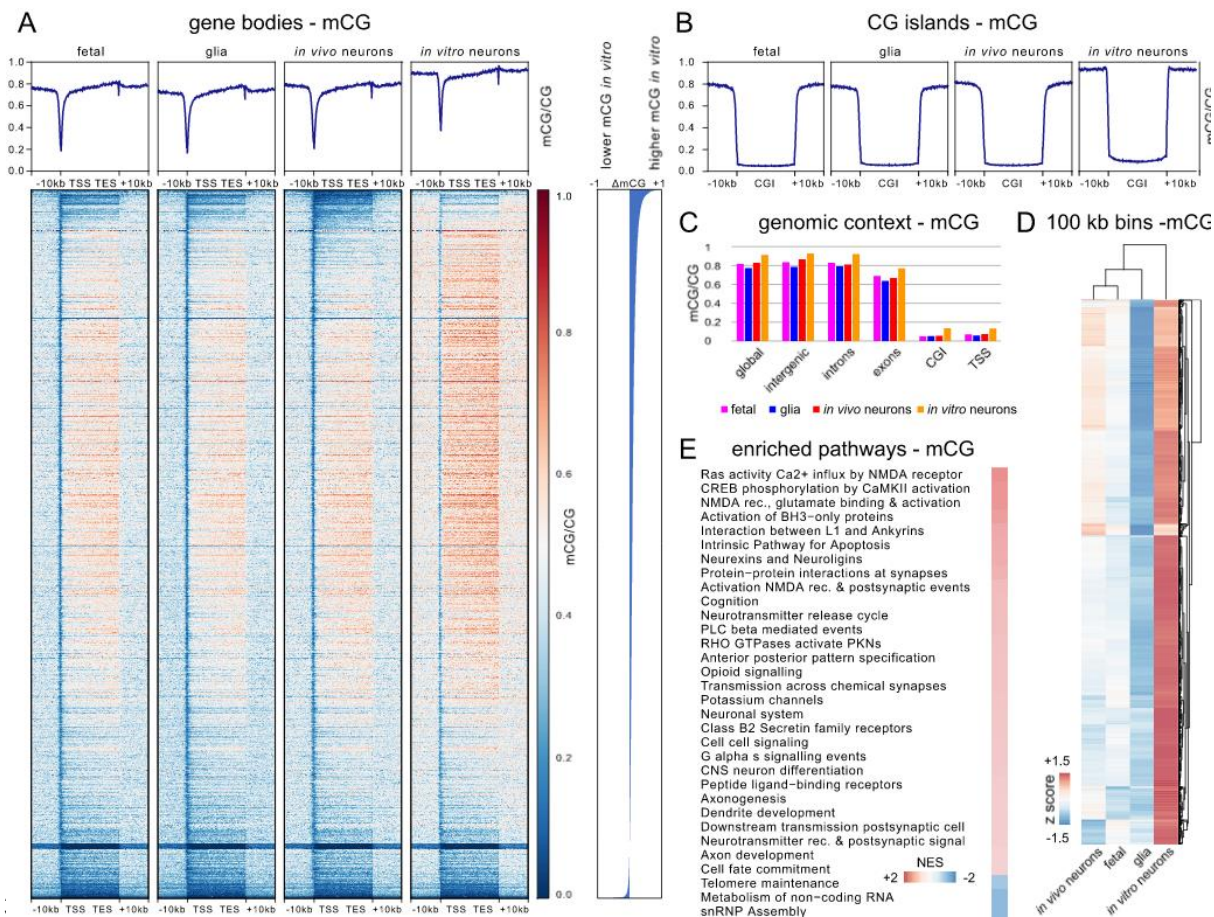
377 In contrast to mouse ESC-derived neurons, only negligible levels of non-CG methylation were
378 observed in any of the human ESC-derived neuronal populations, suggesting that even
379 temporally extended human neuronal cultures are unable to mature sufficiently to acquire
380 mCH. No difference in mCH was detected between shorter, 2-D neuronal cultures, and aged
381 cerebral organoids, suggesting that the culture conditions alone do not promote the acquisition
382 of mCH.

383

384 **Genome wide distribution of mCH and mCG DNA methylation between *in vivo* and**
385 **mESC-derived neurons indicates regional hypermethylation**

386 To establish the degree to which DNA methylation patterns in the ESC-derived
387 neurons recapitulated those of *in vivo* neurons, we generated base resolution methylomes by
388 WGBS and assessed the regional distribution of mCG (Figure 5) and mCH (Figure 6). We
389 then compared this to previously published datasets from 7-week old mouse PFC glial cells
390 (glia) or NeuN-positive neurons (*in vivo* neurons), and fetal mouse frontal cortex (fetal)(Lister
391 et al., 2013), in order to identify potential differences between *in vivo* and *in vitro* neurons
392 (Figures 5 and 6) and the similarities (Figure 7).

393



395 **Figure 5 Global mCG properties of *in vivo* vs *in vitro* generated neurons**

396 mCG characteristics for d38 mESC-derived neurons (*in vitro* neurons), 7-week old mouse
 397 prefrontal cortex neurons (*in vivo* neurons), NeuN-negative cells from 7-week old mouse
 398 prefrontal cortex (glia), and fetal mouse frontal cortex (fetal). **(A)** Weighted methylation levels
 399 (mCG/CG) for all genes and 10 kb flanking regions shown at top. Heatmap shows mCG of
 400 genes and flanking regions sorted by difference in gene body mCG/CG between mESC-
 401 derived neurons and *in vivo* adult mouse PFC neurons, as indicated on the right of the
 402 heatmap. **(B)** Weighted CG methylation level throughout CpG islands (CGIs) for all CGIs and
 403 10 kb flanking regions. **(C)** Weighted methylation levels (mCG/CG) for the whole genome,
 404 intergenic regions, introns, exons, CGIs, and 500 bp flanking transcription start sites (TSS).
 405 **(D)** Hierarchical clustering based on Spearman correlation of mCG levels in all 10 kb bins of

406 the genome. **(E)** Enriched pathways after pre-ranked gene set enrichment analysis based on
407 differences in gene body mCG/CG between *in vivo* and *in vitro* neurons. Shown are top
408 pathways based on enrichment scores (NES) for genes with higher mCG/CG *in vitro* (positive
409 NES score) and lower mCG/CG *in vitro* (negative NES score).

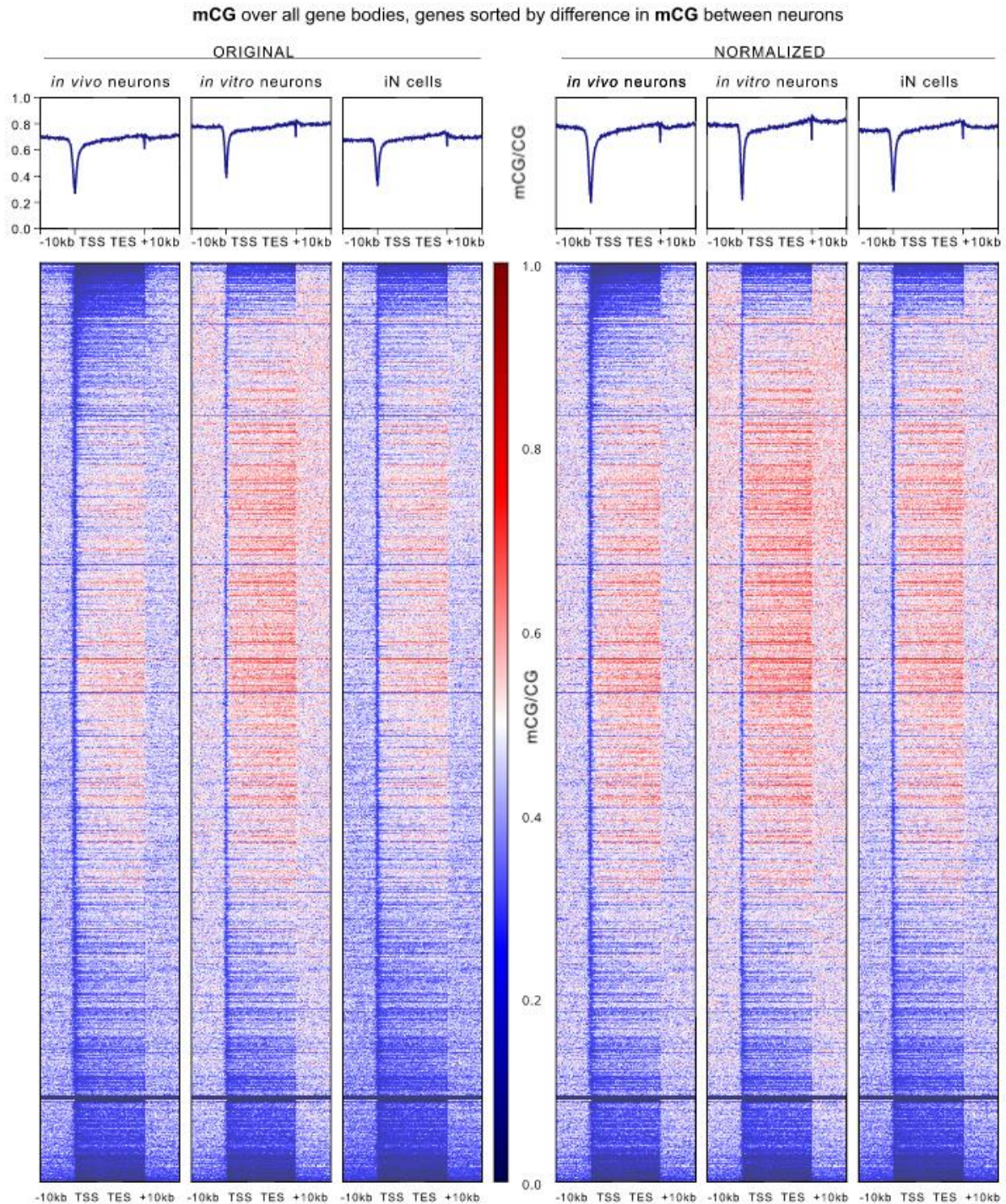
410

411 Analysis of average mCG levels across all gene bodies and associated 10 kb flanking
412 regions (Figure 5A) showed that these were generally similar between fetal, glial and *in vivo*
413 adult neurons, but exhibited a generalised increase in ESC-derived neurons (designated as
414 *in vitro* neurons) (Figures 5A, top plots), consistent with the observed global mCG levels
415 (Figure 4). Analysis of mCH levels (Figure 6A) showed that these were very similar between
416 *in vivo* and *in vitro* neurons, although there was a small localised increase around transcription
417 start sites *in vitro*, and they were much higher than either the glial or fetal samples (Figure 6A,
418 top plot). Genes were subsequently ordered by difference in mean gene body methylation
419 level relative to *in vivo* neurons (Figure 5A and 6A, lower heatmaps). In this analysis, we
420 observed that 38.7% of genes were mCG hypermethylated (gene body $\Delta\text{mCG} > 0.1$) in *in vitro*
421 neurons compared to *in vivo* neurons, while only 0.6% of genes showed mCG
422 hypomethylation ($\Delta\text{mCG} > 0.1$). In the CH context the ratio was more balanced, with 16.0%
423 of genes hypermethylated with $\Delta\text{mCH} > 0.01$, and 12.2% of genes hypomethylated with ΔmCH
424 > 0.01 . Thus, while global and average mCG and mCH gene methylation levels are similar
425 between *in vitro* and *in vivo* neurons, differences in the level of gene body DNA methylation
426 are evident. As a recent study had described DNA methylation patterns in directly
427 reprogrammed mouse neurons (iN cells) (Luo et al., 2019), we also compared our gene body
428 methylation data to the iN cell data (Supplementary Figures 3 - 4). This analysis showed that
429 the hypermethylation of mCG observed in mESC-derived neurons was unique to this
430 developmental model, as both the levels and the patterns observed in iN cells were very similar
431 to those of the *in vivo* neurons (Supplementary Figure 3). For mCH, the overall level of gene
432 body methylation in iN cells was very low (mCH/CH) and lacked the localised spike in

433 methylation observed at TESs *in vivo* and in ESC-derived neurons (Supplementary Figure 4).
434 To directly compare methylation patterns and compensate for the lower overall mCH levels,
435 gene body methylation levels were normalised to the average global methylation level within
436 individual neuron populations. For mCG, despite the slightly lower methylation levels in the iN
437 cells, when methylation patterns were normalised, a higher degree of similarity was observed
438 to the mESC-derived neurons, suggesting that neither *in vitro* neuron population attains genic
439 mCG patterning identical to *in vivo* neurons (Supplementary Figure 3). For mCH, more
440 complex differences were observed, with both iN cells and ESC-derived neurons showing
441 regional variation in the degree of similarity to *in vivo* neurons (Supplementary Figure 4).

442

Martin et al., Supplementary Figure 3



443

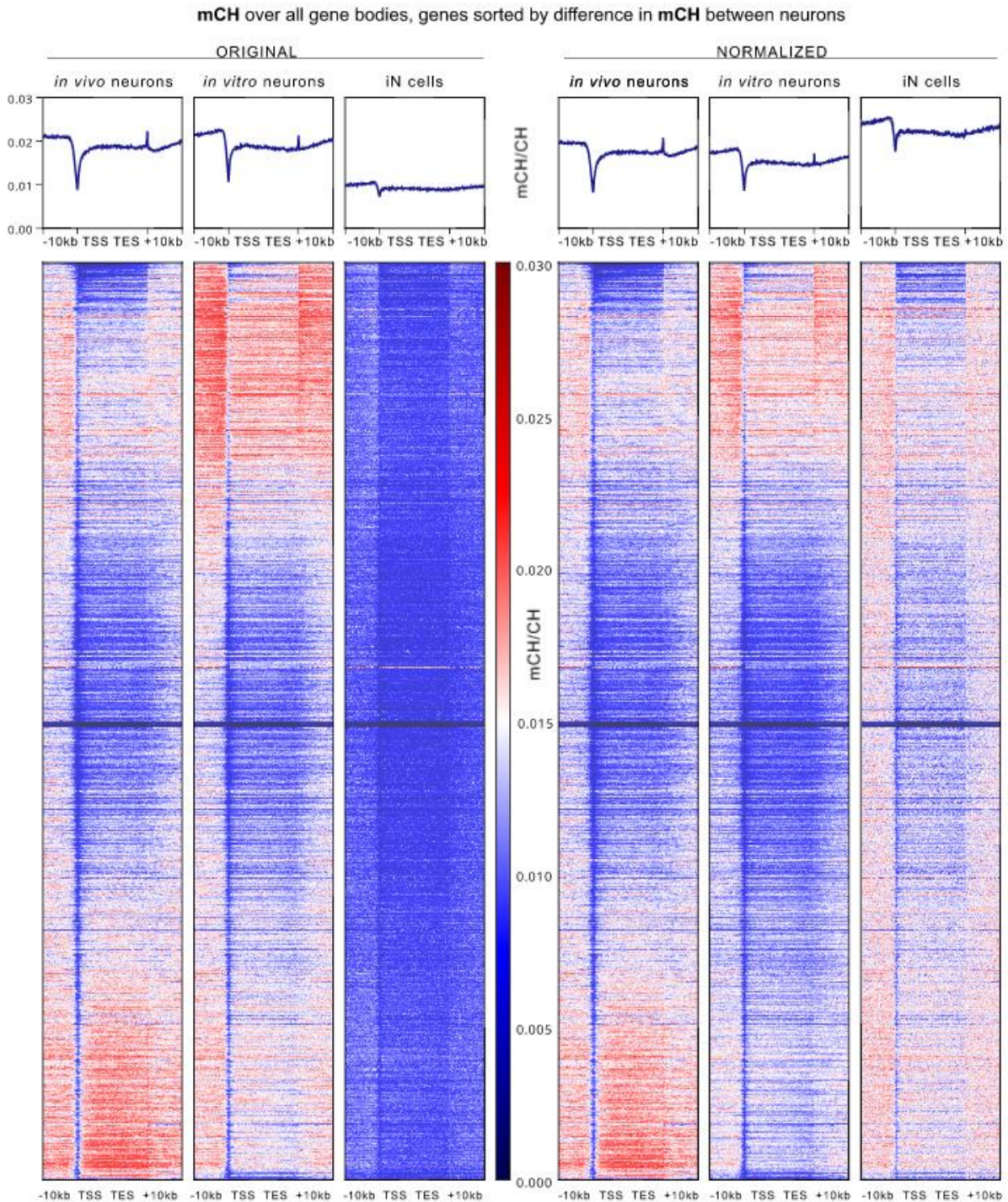
444 **Supplementary Figure 3 DNA methylation in CG context in gene bodies in ESC-derived**

445 **and iN cells compared to in vivo neurons**

446 *Genes in the same order based on CG methylation difference as in Fig 5A but showing CG*
447 *methylation for gene bodies and flanking 10 kb for 7-week adult mouse prefrontal cortex*
448 *neurons (in vivo neurons), mESC-derived neurons (in vitro neurons) and trans-differentiated*
449 *neurons (iN cells) as reported by (Luo et al., 2019). Left side = original data, right side =*
450 *normalized to average global CG methylation levels.*

451

Martin et al., Supplementary Figure 4



452

453 ***Supplementary Figure 4 DNA methylation in CH context in gene bodies in ESC-derived***

454 ***and iN cells compared to in vivo neurons***

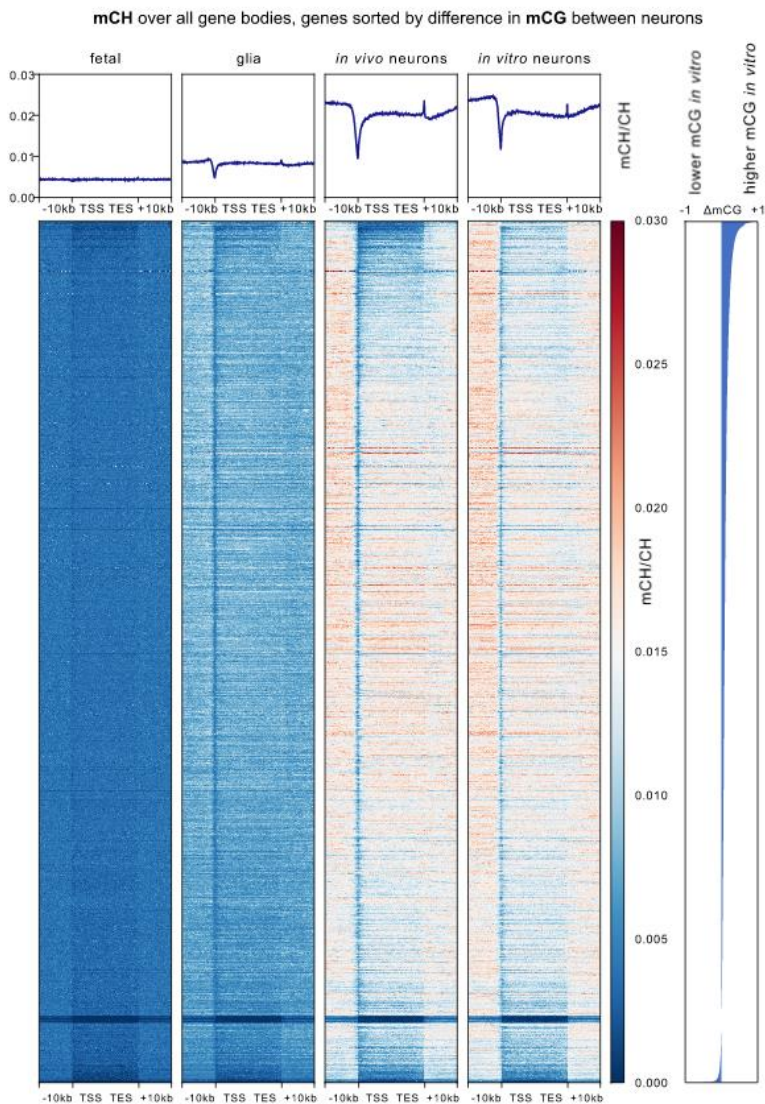
455 *Genes in the same order based on CH methylation difference as in Fig 6A but showing CH*
456 *methylation for gene bodies and flanking 10 kb for 7-week adult mouse prefrontal cortex*
457 *neurons (in vivo neurons), d38 mESC-derived neurons (in vitro neurons) and trans-*
458 *differentiated neurons made from fibroblasts (iN cells) as reported by (Luo et al., 2019). Left*
459 *side = original data, right side = normalized to average global CH methylation levels.*

460

461

462

Martin et al., Supplementary Figure 5



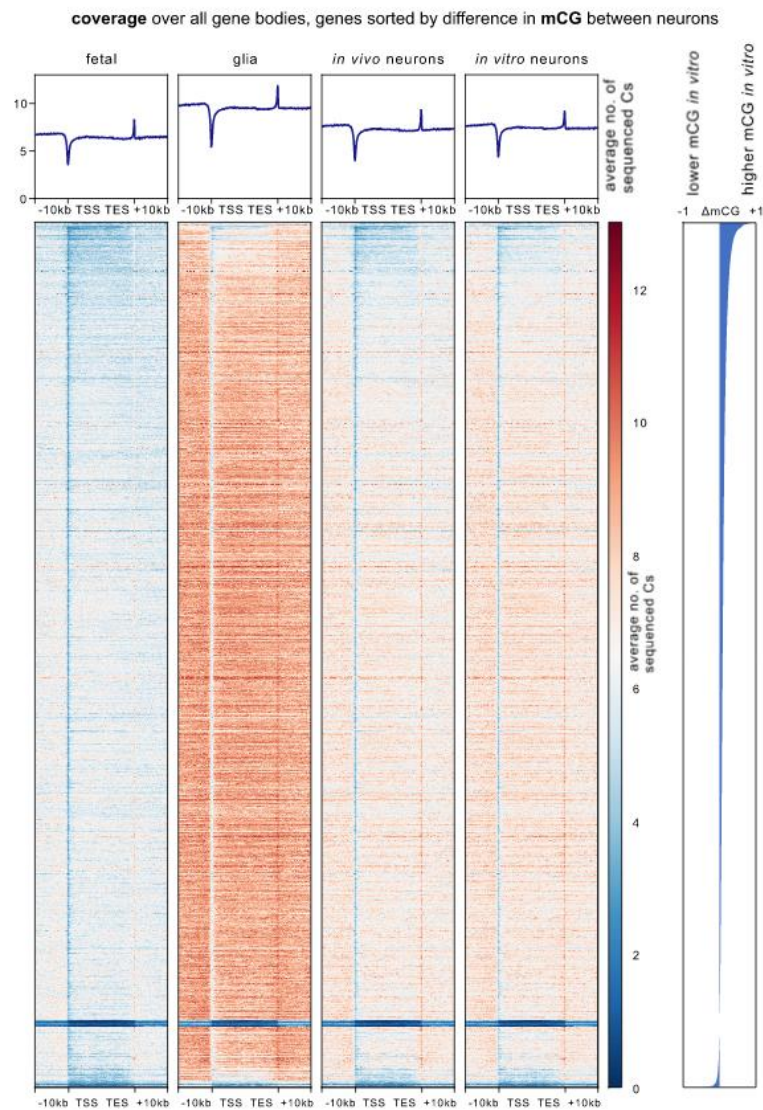
463

464 **Supplementary Figure 5 DNA methylation in CH context in gene bodies sorted for**
465 **differences in mCG between neuronal samples**

466 *Genes in the same order based on CG methylation difference as in Fig 5A but showing CH*
467 *methylation for gene bodies and flanking 10 kb for fetal mouse frontal cortex (fetal), NeuN-*
468 *negative cells from 7-week adult mouse prefrontal cortex (glia), 7-week adult mouse prefrontal*
469 *cortex neurons (in vivo neurons), and d38 mESC-derived neurons (in vitro neurons).*
470 *Difference in mCG between both neuronal samples used for gene order is shown on the right*

471

Martin et al., Supplementary Figure 6



472

473

474 **Supplementary Figure 6 Cytosine coverage in gene bodies sorted for differences in**
475 **mCG between neuronal samples**

476 *Genes are in the same order based on CG methylation difference as in Fig 5A but showing*
477 *average number of covered cytosines per bin for gene bodies and flanking 10 kb for fetal.*
478 *mouse frontal cortex (fetal), NeuN-negative cells from 7-week adult mouse prefrontal cortex*

479 (*glia*), 7-week adult mouse prefrontal cortex neurons (*in vivo* neurons), and d38 mESC-derived
480 neurons (*in vitro* neurons). Difference in mCG between both neuronal samples used for gene
481 order is shown on the right.

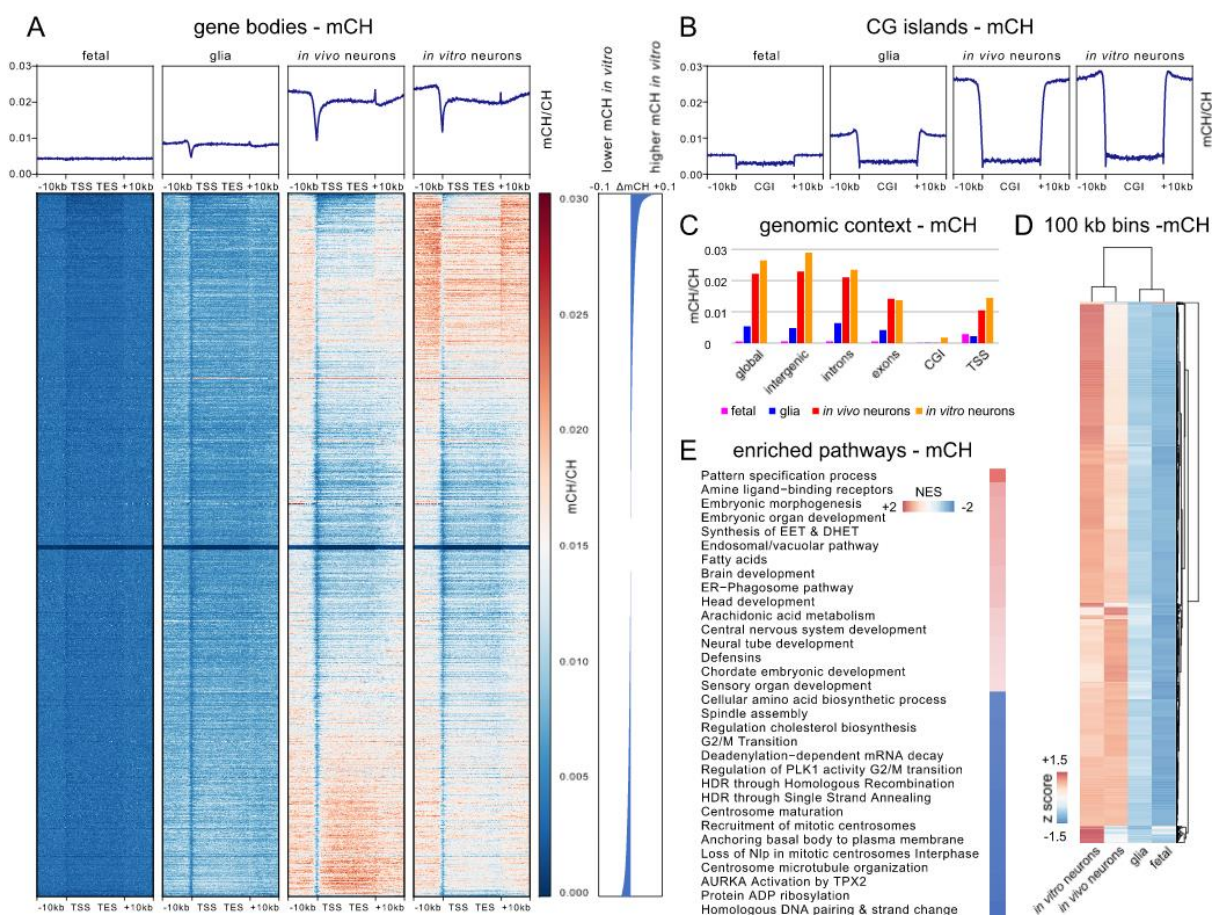
482

483 To investigate the relationship between mCG and mCH within gene bodies in the ESC-
484 derived neurons, we assessed mCH patterns over all genes ordered by gene body mCG
485 difference (*in vitro* neuron mCG - *in vivo* neuron mCG; Supplementary Figure 5), and gene
486 body mCG patterns over all genes ordered by gene body mCH difference (*in vitro* neuron mCH
487 - *in vivo* neuron mCH; Supplementary Figure 7). These analyses revealed that the patterns of
488 DNA methylation levels observed were different for each context (Figure 5A and 6A). Indeed
489 a very low Pearson correlation of differences in methylation for both contexts between ESC-
490 derived neurons and *in vivo* neurons ($r = 0.0688$) suggests that independent processes define
491 DNA methylation levels for each context, and that individual genes are methylated to a
492 different degree by mCG and mCH, compared to the global average levels. Plotting the total
493 number of calls at cytosine reference positions within gene bodies in the same order confirmed
494 that the observed differences are not a result of different sequencing coverage between
495 samples (Supplementary Figures 6 and 8).

496 In mESC-derived neurons, a marginal and consistent increase in mCG was observed
497 within and flanking CpG islands (CGIs), regions that are normally depleted of methylation
498 (Schubeler, 2015) (Figure 5B). Similarly, there was a slight increase in mCH methylation within
499 CGIs. However, there was a pronounced and localised increase in the level of mCH in the
500 regions immediately flanking CGIs (Figure 6B), suggesting that methylation of CG and CH
501 sites in these regions are regulated differently. In order to assess whether particular genomic
502 features exhibited different methylation levels in mESC-derived neurons, we measured the
503 weighted methylation levels (mCG/CG or mCH/CH) in intergenic regions, introns, exons, and
504 500 bp upstream and downstream of transcription start sites (Figures 5C and 6C). This

505 revealed genome-wide CG hypermethylation in mESC-derived neurons (~6-12% higher than
 506 in *in vivo* neurons, absolute methylation level difference), suggesting a generalised
 507 dysregulation of methylation level, while increased mCH was observed in all genomic features
 508 except exons. The reason for the specific exclusion of exons from hypermethylation in the
 509 mCH context is unknown but suggests that specialised mechanisms regulating exonal mCH
 510 levels are conserved *in vitro*.

Martin et al., Figure 6



511

512 **Figure 6 Global mCH properties of *in vivo* vs *in vitro* generated neurons**

513 *mCH* characteristics for d38 mESC-derived neurons (*in vitro* neurons), 7-week old mouse
 514 prefrontal cortex neurons (*in vivo* neurons), NeuN-negative cells from 7-week old mouse
 515 prefrontal cortex (glia), and fetal mouse frontal cortex (fetal). **(A)** Weighted methylation levels
 516 (*mCH/CH*) for all genes and 10 kb flanking regions shown at top. Heatmap shows *mCH* of

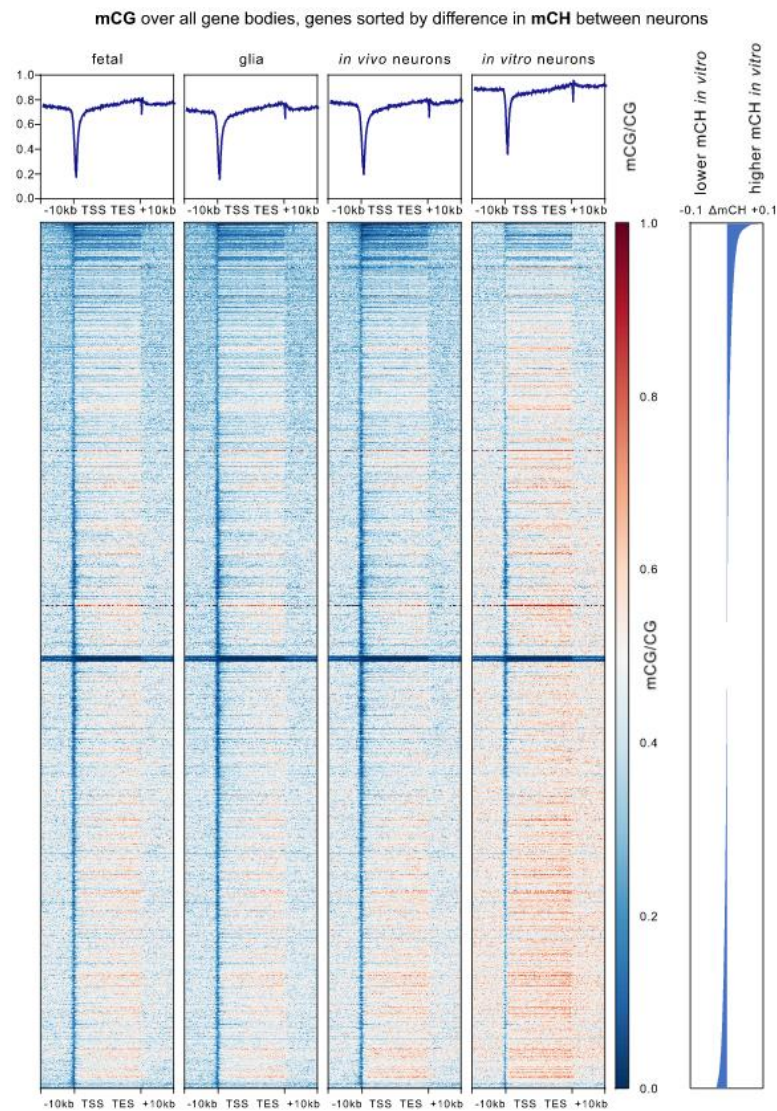
517 *genes and flanking regions sorted by difference in gene body mCH/CH between mESC-*
518 *derived neurons and in vivo adult mouse PFC neurons, as indicated on the right of the*
519 *heatmap. (B) Weighted CH methylation level throughout CpG islands (CGIs) for all CGIs and*
520 *10 kb flanking regions. (C) Weighted methylation levels (mCH/CH) for the whole genome,*
521 *intergenic regions, introns, exons, CGIs, and 500 bp flanking TSSs. (D) Hierarchical clustering*
522 *based on Spearman correlation of mCH levels in all 10 kb bins of the genome. (E) Enriched*
523 *pathways after pre-ranked gene set enrichment analysis based on differences in gene body*
524 *mCH between in vivo and in vitro neurons. Shown are top pathways based on enrichment*
525 *scores (NES) for genes with higher mCH/CH in vitro (positive NES score) and lower mCH/CH*
526 *in vitro (negative NES score).*

527

528 Next, we assessed regional correlation in mCG and mCH levels in 100 kb bins of the
529 whole genome (excluding chromosomes X and Y) between mESC-derived neurons, fetal
530 frontal cortex, and 7-week old mouse PFC neurons and glia (Figure 5D and 6D). For mCG,
531 fetal brain and adult neurons were the most similar, with adult glia joining at the next node,
532 while mESC-derived neurons formed their own branch. The low correlation between neuronal
533 samples is likely due to the overall higher methylation of CG in ESC-derived neurons. For
534 mCH, there was a high similarity between *in vitro*- and *in vivo*-derived neuronal datasets, while
535 glia were similar to the fetal sample, consistent with the neuron-specific accumulation of mCH.
536 This clustering based on bins also showed that differences in methylation between neurons
537 were not evenly distributed throughout the genome but show regional variability.

538

Martin et al., Supplementary Figure 7



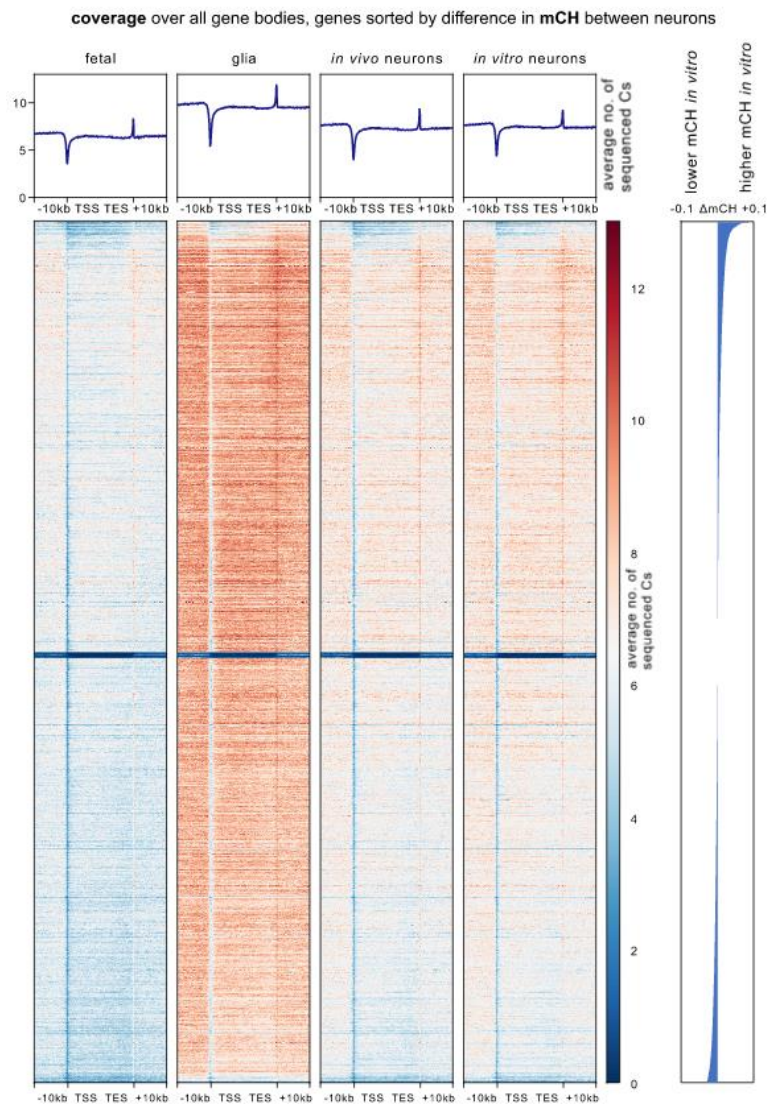
539

540 **Supplementary Figure 7 DNA methylation in CG context in gene bodies sorted for**
541 **differences in mCH between neuronal samples**

542 *Genes are in the same order based on CH methylation difference as in Fig 5B but showing*
543 *CG methylation for gene bodies and flanking 10 kb for fetal mouse frontal cortex (fetal), NeuN-*
544 *negative cells from 7-week adult mouse prefrontal cortex (glia), 7-week adult mouse prefrontal*
545 *cortex neurons (in vivo neurons), and d38 mESC-derived neurons (in vitro neurons).*
546 *Difference in mCH between both neuronal samples used for gene order is shown on the right.*

547

Martin et al., Supplementary Figure 8



548

549 **Supplementary Figure 8 Cytosine coverage in gene bodies sorted for differences in**
550 **mCH between neuronal samples**

551 *Genes are in the same order based on CH methylation difference as in Fig 5B but showing*
552 *average number of covered cytosines per bin for gene bodies and flanking 10 kb for fetal*
553 *mouse frontal cortex (fetal), NeuN-negative cells from 7-week adult mouse prefrontal cortex*
554 *(glia), 7-week adult mouse prefrontal cortex neurons (in vivo neurons), and d38 mESC-derived*
555 *neurons (in vitro neurons). Difference in mCH between both neuronal samples used for gene*
556 *order is shown on the right.*

557

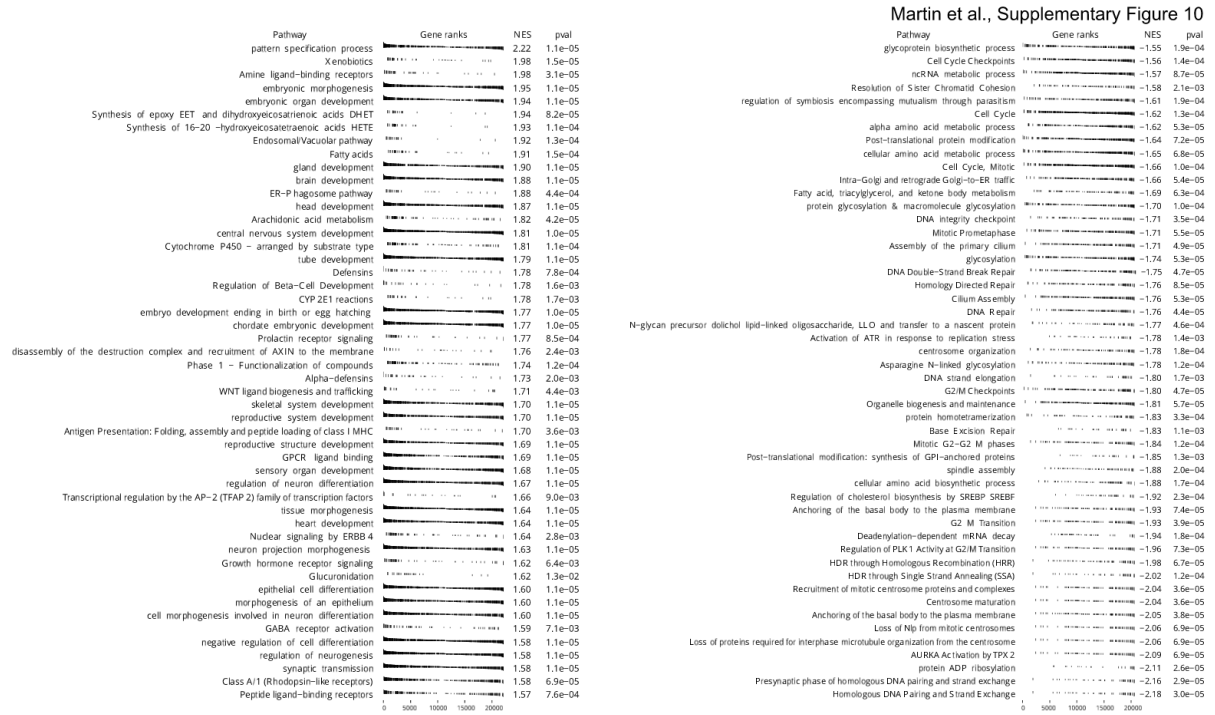
558 Finally, we generated ranked lists of genes based on either similarity or difference in genic
559 methylation between neuronal populations and performed gene set enrichment analysis
560 (GSEA) to examine correlation with biologically relevant pathways. We composed a pathway
561 package by combining gene ontology as well as reactome pathway datasets and performed
562 GSEA on both gene lists. Initially, we performed GSEA based on differences in methylation
563 levels (Figure 5E and 6E). For mCG, top pathways with higher gene body methylation *in vitro*
564 represented neuronal activity and synapse formation. Due to the generalised
565 hypermethylation in the CG context, relatively few pathways were enriched for genes with
566 lower methylation values (at $p < 0.05$, Figure 5E), none of which directly related to neurons. Full
567 details of the top 50 hyper- and hypomethylated pathways for mCG context are listed in
568 Supplementary Figure 9. For mCH, top pathways enriched for genes hypermethylated in *in*
569 *vitro* neurons included morphogenesis and development, including brain and central nervous
570 system development. However, unlike mCG, differences in neuronal activity and synapse
571 formation were not detected. Genes hypomethylated in the mCH context in *in vitro* neurons
572 included pathways for cell cycle, cell division and DNA repair, but again, no pathways relating
573 directly to neurons were identified (Figure 6E). Full details for the top 50 of hyper- and
574 hypomethylated pathways for mCH context are listed in Supplementary Figure 10. To
575 simultaneously identify gene sets that share similar methylation states in both *in vitro* and *in*
576 *vivo* neuron populations and discriminate them against fetal or glial cells, we applied GSEA
577 on genes ranked by a combination of similarity between the mESC-derived *in vitro* neurons
578 and *in vivo* neurons, and dissimilarity to non-neuronal cell types (glia and fetal brain cells,
579 Figure 7). This analysis was performed for mCG and mCH independently and resulted in an
580 enrichment for pathways linked to genes that have an equivalent methylation



581

582 **Supplementary Figure 9 Top 50 enriched pathways for genes differentially methylated**
 583 **in CG context between in vitro neurons and in vivo neurons**

584 Pathways were ranked by enrichment score (NES), whereas positive NES indicates pathways
 585 enriched in genes hypermethylated for CG in in vitro neurons, while negative NES indicates
 586 pathways enriched in hypomethylated genes. Gene rank plots show position of genes being
 587 part of a pathway set within the ordering of all genes based on methylation difference in mCG.
 588 Pathways with p value larger than 0.05 shown in red.



589

590 **Supplementary Figure 10 Top 50 enriched pathways for genes differentially methylated**
 591 **in CH context between in vitro neurons and in vivo neurons**

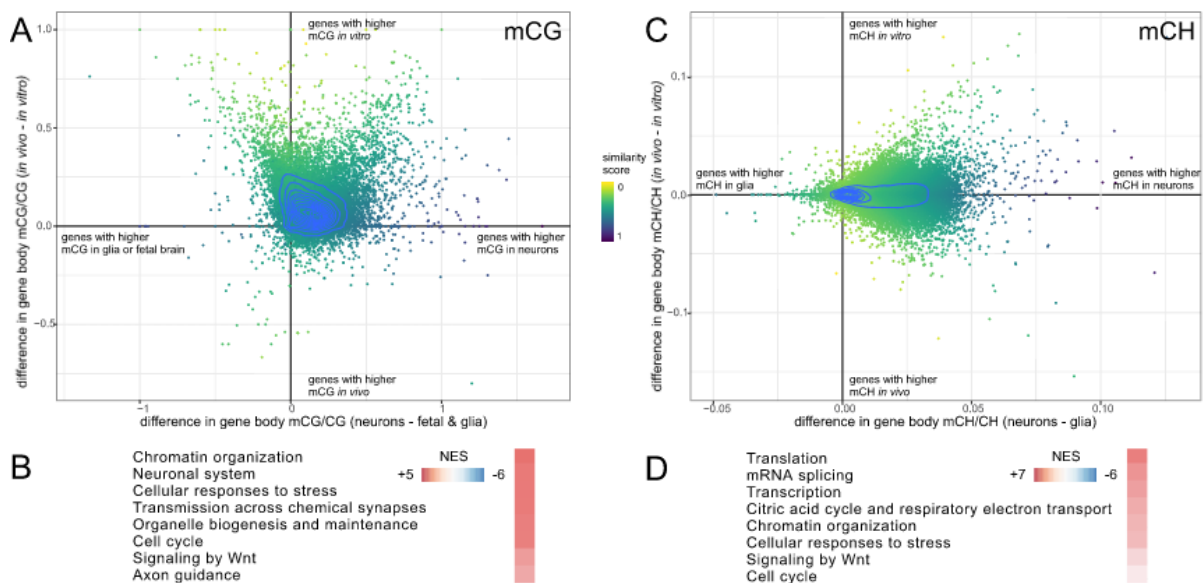
592 Pathways were ranked by enrichment score (NES), whereas positive NES indicates pathways
 593 enriched in genes hypermethylated for CH in in vitro neurons, while negative NES indicates
 594 pathways enriched in hypomethylated genes. Gene rank plots shows the position of genes
 595 being part of a pathway set within the ordering of all genes based on methylation difference in
 596 mCH.

597

598 state in both of the neuronal samples. It is important to note that this analysis enriches for
 599 similarity irrespective of overall methylation levels, whether high or low. When considering
 600 mCG, the most represented pathways belonged to two major groups: neuronal function or cell
 601 cycle. While neuronal terms are expected to be shared between neurons, the enrichment of
 602 the latter group is likely due to its associated genes having a different methylation state in
 603 post-mitotic neurons, compared to actively proliferating cells. Interestingly for mCH, with the

604 exception of Wnt signalling, the most highly enriched pathways did not relate directly to
 605 neurons, but included pathways related to chromatin organization, transcription and splicing
 606 (Figure 7 and Supplementary Figure 9). Together with the observed differential localisation of
 607 mCG and mCA in neuronal nuclei, this data suggests that rather than being directly involved
 608 in neuronal specification, mCH could play a role in the dynamic reorganisation of chromatin
 609 (Fraser et al., 2015) and the regulation of alternative splicing that occurs during neuronal
 610 maturation (Hubbard et al., 2013, Weyn-Vanhenteryck et al., 2018).

Martin et al., Figure 7



611

612 **Figure 7 Enrichment for genes with similar methylation patterns in in vitro neurons and**
 613 **in vivo neurons**

614 **(A)** Differences in gene body mCG level between neurons and fetal brain as well as glia (x-
 615 axis), and differences in gene body mCG level between both neuronal populations (y-axis),
 616 for all 24,049 genes with WGBS coverage. Dots are coloured by the similarity score that was
 617 used for gene set enrichment. Blue contour plot is based on gene density. **(B)** Selection of top
 618 enriched pathways from GSEA using similarity scoring from mCG information. **(C)** Differences
 619 in gene body mCH level between neurons and glia (x axis), and differences in gene body mCH
 620 level between both neuronal populations (y-axis), for all 24,049 genes with WGBS coverage.

621 **(D)** Selection of top enriched pathways from GSEA using similarity scoring from mCH
 622 information. Full details for the top 20 similarity-enriched pathways are listed in Supplementary
 623 Figure 11.

624

Martin et al., Supplementary Figure 11

	Pathway	Gene ranks	NES	pval
mCG	Chromatin organization		4.27	1.1e-05
	Neuronal system		4.09	1.0e-05
	Cellular responses to stress		4.07	1.1e-05
	Transmission across chemical synapses		4.05	1.1e-05
	Organelle biogenesis and maintenance		3.95	1.0e-05
	Cell cycle		3.93	1.0e-05
	M phase		3.84	1.1e-05
	Transcription		3.68	1.1e-05
	Assembly of the primary cilium		3.58	1.1e-05
	Translation		3.51	1.1e-05
	Signaling by Wnt		3.26	1.1e-05
	TCF dependent signaling in response to Wnt		3.21	1.1e-05
	Signaling by Rho GTPases		3.17	1.0e-05
	Mitotic anaphase		3.16	1.1e-05
	separation of sister chromatids		3.06	1.1e-05
	Mus musculus biological processes		3.00	1.1e-05
	Axon guidance		2.97	1.0e-05
	Post-translational protein modification		2.97	1.0e-05
	Developmental biology		2.77	1.0e-05
	Signalling by NGF		2.75	1.0e-05
		0 5000 10000 15000 20000		
mCH	Translation		6.62	1.1e-05
	mRNA splicing		5.72	1.2e-05
	Transcription		5.30	1.1e-05
	Citric acid TCA cycle and respiratory electron transport		4.89	1.2e-05
	Chromatin organization		4.55	1.1e-05
	Cellular responses to stress		4.36	1.1e-05
	Organelle biogenesis and maintenance		3.93	1.1e-05
	Cellular senescence		3.64	1.2e-05
	Membrane trafficking		3.54	1.1e-05
	TCF dependent signaling in response to Wnt		3.47	1.1e-05
	Signaling by Wnt		3.34	1.1e-05
	C-type lectin receptors CLR		3.19	1.2e-05
	M phase		3.04	1.1e-05
	Cell cycle checkpoints		2.99	1.2e-05
	Assembly of the primary cilium		2.96	1.1e-05
	Cell cycle		2.74	1.0e-05
	Programmed cell death		2.74	1.1e-05
	S phase		2.69	1.2e-05
	Signaling by Hedgehog		2.68	1.2e-05
	Mus musculus biological processes		2.55	1.1e-05
		0 5000 10000 15000 20000		

625

626 **Supplementary Figure 11 Enriched pathways for genes with similar methylation**
 627 **patterns for in vitro neurons and in vivo neurons**

628 Pathways were ranked by enrichment score (NES), based on similarity between in vitro and
 629 in vivo neurons and dissimilarity to glia and fetal brain in mCG and mCH context respectively.
 630 Gene rank plots show the position of genes being part of a pathway set within the ranking of
 631 all genes.

632

633 Discussion

634 The complex dynamics, composition, and patterns of DNA methylation observed in the
635 development and maturation of postnatal neurons is hypothesized to play an important role in
636 modifying gene expression and consolidating both neuronal cell types and their response to
637 activity (Cortes-Mendoza et al., 2013, Day et al., 2013, Feng and Fan, 2009, Graff et al., 2012,
638 Miller and Sweatt, 2007, Stroud et al., 2017). Mouse studies have identified some factors
639 involved in the process, including the DNA methyltransferases catalysing the deposition of mC
640 (Guo et al., 2014, Nguyen et al., 2007), and methylation readers such as MeCP2 that link DNA
641 methylation to gene expression (Chen et al., 2015, Fasolino and Zhou, 2017, Kinde et al.,
642 2016, Lager et al., 2017, Mellen et al., 2012, Skene et al., 2010, Stroud et al., 2017).
643 However, many basic questions remain unanswered, including the roles and regulation of
644 dynamic methylation events, and the factors that define the targeting of methylation sites.
645 Developing a robust *in vitro* model system to recapitulate the diverse methylation events
646 particular to neurons is important to facilitate the detailed molecular dissection of these
647 processes. In the present study we have extended an established protocol to differentiate
648 cortical neurons from mESCs and shown that these cells acquire *in vivo* levels of non-CG
649 methylation in a similar time frame to *in vivo* brain development. Furthermore, we have shown
650 that the timing of mCH deposition *in vitro* correlates to a transient increase in *Dnmt3a*
651 expression, which also recapitulates that observed *in vivo* (Lister et al., 2013). If, as these
652 results suggest, the deposition of mCH and *Dnmt3a* expression is indeed hardwired into the
653 developmental process, this has profound implications for studying the equivalent processes
654 in human iPSC-derived neurons. The human brain has a much more extended developmental
655 timeline compared to mouse (Stiles and Jernigan, 2010), and maximal *in vivo* mCH
656 methylation levels are not observed until late adolescence (16+ yr) (Lister et al., 2013). The
657 most advanced *in vitro* human cerebral organoid differentiation protocols currently available
658 can only recapitulate relatively early embryonic developmental stages (reviewed (Benito-
659 Kwiecinski and Lancaster, 2019)). Whether further development of human cerebral organoids

660 through *in vitro* vascularisation (Cakir et al., 2019) or transplantation into the mouse (Mansour
661 et al., 2018) can overcome this developmental obstacle and accelerate human neuron
662 maturation to experimentally tractable time scales is currently unknown. To our knowledge,
663 the mouse data presented here is the first report of mammalian neurons derived *in vitro* from
664 pluripotent cells that harbor mCH at levels similar to those present in neurons *in vivo*, and
665 opens the door to further, targeted investigations of the regulatory pathways and
666 environmental factors involved.

667 Detailed analysis of DNA methylation levels and genomic distribution in mouse ESC-
668 derived neurons identified several interesting features. Firstly, the levels and distribution of
669 mCG and mCH were regulated independently. Compared to the mouse brain neurons,
670 generalised hypermethylation in the mCG context, both within gene bodies and across the
671 genome, was not observed for mCH, which showed relatively normal gene body methylation
672 levels and slightly lower exon methylation. Regions of higher methylation in CG context were
673 not in general accompanied by higher methylation in CH context and *vice versa*, and regions
674 showing comparably lower methylation in one context did not show the same pattern in the
675 other context. These observations suggest that different regulatory mechanisms are involved
676 in the remodelling of neuron methylation patterns during maturation, depending upon the DNA
677 context and genomic feature targeted. As the mESC-derived neurons did not recapitulate
678 either of these methylation contexts with complete fidelity, it is likely that other factors, such
679 as environment, neuronal connectivity and activity, all act to develop the mature neuronal
680 methylome. Similarly, our comparisons to previously published iN cell data (Luo et al., 2019)
681 suggest that in this model system also, other factors are required to fully develop *in vivo*
682 methylation levels and patterns.

683 The early post-natal nuclear landscape of neurons is highly dynamic, with changes in
684 gene transcription (Kang et al., 2011), alternative splicing (Furlanis and Scheiffele, 2018,
685 Weyn-Vanhentenryck et al., 2018), DNA methylation (He and Ecker, 2015, Lister et al., 2013,
686 Szulwach et al., 2011), and chromatin remodelling (Gallegos et al., 2018). It is likely that the

687 regulation of all these facets of neuron development are tightly interconnected. It is well-
688 established that gene body mCH levels in neurons is inversely correlated with gene expression
689 (Chen et al., 2015, Chen et al., 2014, Gabel et al., 2015, Lister et al., 2013), and it has been
690 suggested that establishment of early post-natal mCH regulates the transcription of affected
691 genes at later time points (Stroud et al., 2017). Immunologically labelled mCA, both *in vivo*
692 and *in vitro*, shows a strong association with the nuclear periphery, suggesting association of
693 these genomic regions with the nuclear lamina. As the nuclear lamina forms a repressive
694 environment for transcription (Zuleger et al., 2011), association and dissociation of genes with
695 this environment can be a potent regulator of expression. During the neural induction of
696 mESCs, the pro-neural gene *MASH1* is translocated away from the nuclear lamina,
697 concomitant with upregulation of its expression (Williams et al., 2006). Similarly, hundreds of
698 genes change lamina interactions during differentiation from mESC to neural progenitor cells,
699 and subsequently to astrocytes, and genes affected by altered lamina interactions reflect cell
700 identity and influence the likelihood of a gene being subsequently activated (Peric-Hupkes et
701 al., 2010). These findings suggest that lamina-genome interactions are centrally involved in
702 the control of gene expression programs during lineage commitment and terminal
703 differentiation. The association and dissociation of genes from the nuclear lamina is not
704 restricted to developing or differentiating cells. For example, the *BDNF* gene is translocated
705 away from the nuclear lamina, with a concomitant increase in expression, following stimulation
706 of mature neurons *in vivo*, proving that transcription-associated gene repositioning can occur
707 in adult neurons, as a result of enhanced activity (Walczak et al., 2013). While it is not yet
708 known how mCA associates with the nuclear lamina, or whether this is a direct association,
709 one possibility could involve binding to MeCP2 (Chen et al., 2015, Gabel et al., 2015, Lister et
710 al., 2013, Stroud et al., 2017). MeCP2 is a multifunctional protein, with reported roles in both
711 repression and upregulation of gene expression, as well as involvement in nuclear structure
712 (Chahrour and Zoghbi, 2007, Lager et al., 2017, Young et al., 2005). In addition to binding
713 various methylated DNA species through its methyl-binding domain, including mCA, mCG,
714 and 5hmC (Chen et al., 2015, Gabel et al., 2015, Guo et al., 2014, Lager et al., 2017), MeCP2

715 is able to interact directly with the lamin-B receptor (Guarda et al., 2009), a role that is
716 independent of its function as an epigenetic reader protein. As levels of MeCP2 are very high
717 in neurons, approaching that of H1 linker histone levels (Kishi and Macklis, 2004, Skene et al.,
718 2010), it is tempting to speculate that one role of MeCP2 binding to mCA is to regulate its
719 association with the nuclear lamina. The level of MeCP2 has been shown to increase during
720 mESC-derived neuron differentiation (Yazdani et al., 2012) consistent with a close regulatory
721 association to the increased levels of mCA observed here.

722 Generation of base resolution DNA methylomes of mESC-derived neurons allowed us
723 to compare pathways for which gene sets showed either the greatest similarity or the greatest
724 difference in methylation levels to *in vivo* neurons. Pathways hypermethylated in the mCH
725 context in ESC-derived neurons relative to *in vivo* neurons included a range of broad
726 developmental pathways, with no particular emphasis on neuron maturation or function. As
727 mCH has been shown to be deposited in the bodies of lowly expressed genes (Stroud et al.,
728 2017), this suggests that these pathways have reduced functionality in post-mitotic ESC-
729 derived neurons. In contrast, pathways with hypomethylation in the mCH context represented
730 the cell cycle and mitosis. These pathways are predicted to be silenced in post-mitotic cells,
731 suggesting that this hypomethylation occurs as a result of the inclusion of the represented
732 genes in tightly packed heterochromatin, although further studies are needed to confirm this.
733 Taken together, these data suggest that despite the different levels and labeling patterns for
734 mCH in the mESC-derived neurons, some fidelity is retained in the ESC-derived cells.
735 Interestingly, gene set enrichment pathways showing the greatest similarity in mCH between
736 *in vivo* and ESC-derived neurons include a range of regulatory pathways involved in
737 transcription, splicing and chromatin organisation, all aspects of neuron development that are
738 significantly modified in early postnatal neurons. Whether mCH is involved in the regulation of
739 alternative splicing or chromatin remodelling in neurons remains to be determined. However,
740 direct links between mCA and alternative splicing have been shown in human ESCs (Tan et
741 al., 2019) and CG methylation contributes to the inclusion or exclusion of alternatively spliced

742 exons in human cell lines (Maunakea et al., 2013). Furthermore, as MeCP2 can also be
743 associated with alternative splicing and nuclear architecture (Yazdani et al., 2012, Young et
744 al., 2005), a potential role for mCH in these processes should be considered.

745 The generalised CG hypermethylation in mESC-derived neurons challenged the
746 analysis of gene sets enriched for either similarity or difference to *in vivo* neurons, as the
747 highest ranked gene sets for both analyses represented different but closely related aspects
748 of neuron development and function. The mechanism underlying mCG hypermethylation is
749 not yet known. It could reflect either increased methylation, decreased activity of
750 demethylation pathways (Wu and Zhang, 2017), or an accumulation of 5hmC (Lister et al.,
751 2013, Szulwach et al., 2011). or a combination of any or all three. The genome-wide increase
752 in mCG was observed to occur earlier in the neuron differentiation timeline than the maximal
753 increase in mCH, suggesting that these two processes are regulated independently.

754 Together, this work establishes that *in vitro* differentiation of mouse embryonic cells to
755 neurons is a highly tractable and valuable model system with which to further dissect the roles
756 of DNA methylation and higher order intranuclear architecture on neuron maturation and
757 function.

758

759 **Materials and Methods**

760 *Reagents and Antibodies*

761 Primary antibodies are detailed in Supplementary Table 1. Directly-conjugated Alexa488-
762 mouse anti-NeuN was from Millipore (MAB377X). Mouse monoclonal antibodies to 5-
763 methylcytosine-adenosine dinucleoside (mCA) and 5-methylcytosine-guanine dinucleoside
764 (mCG) were raised against KLH-conjugated dinucleosides at the Technology Development
765 Laboratory (Babraham Bioscience Technologies Ltd, Cambridge, UK) (anti-mCA antibody
766 clone 2C8H8A6 currently available from Active Motif, Cat. No 61783/4). Alexa Fluor secondary

767 antibodies were purchased from Life Technologies. ESGRO recombinant mouse Leukaemia
768 Inhibitory Factor (LIF) was obtained from Merck Millipore. The remaining reagents were
769 obtained from ThermoFisher Scientific or Sigma Aldrich unless otherwise specified.

770

771 *Mouse Tissue Collection and in vitro neuron differentiation*

772 Adult C57BL/6 mice (8-10 weeks old) were sacrificed and brains dissected and snap frozen
773 on dry ice. Brains were then sectioned on a cryostat at 12 microns, placed on poly-L-lysine
774 slides (VWR) and stored at -80°C until processing. All experimental procedures were approved
775 by the Animal Welfare, Experimentation and Ethics Committee at the Babraham Institute and
776 were performed under licenses by the Home Office (UK) in accordance with the Animals
777 (Scientific Procedures) Act 1986.

778 For primary neurons, hippocampal or cortical neurons were cultured from embryonic
779 day 18 C57BL/6 mouse brains as described previously (Lanoue et al., 2017). All procedures
780 were conducted according to protocols and guidelines approved by the University of
781 Queensland Animal Ethics Committee. Isolated E18 neural progenitors were either frozen
782 directly for WGBS (E18 samples) or plated onto 0.1 mg/ml Poly L-Lysine / 8 µg/ml laminin-
783 coated plates in Neurobasal containing 2% B27, 0.5 mM L-glutamine and 1% Pen-Strep and
784 maintained for 14 days. 14DIV neurons were either dissociated with Accutase and frozen as
785 cell pellets for WGBS or washed in PBS and fixed in 2% PFA/PBS for ICC.

786

787 *Murine embryonic stem cell culture and in vitro neuron differentiation*

788 Two mESC cells lines, R1 (ATCC SCRC-1011) derived from a 129X1 x 129S1 male
789 blastocyst (Nagy et al., 1993) and G4 derived from a 129S6/SvEvTac x C57BL/6Ncr male
790 blastocyst (George et al., 2007), were maintained on gamma-irradiated mouse embryonic

791 fibroblasts in mESC medium (Dulbecco's Modified Eagle Medium (DMEM) (GIBCO), 15%
792 Hyclone defined FBS (GE Healthcare), 10³U/ml ESGRO LIF (Millipore), 1x L-Glutamax, 1x
793 sodium pyruvate, NEAA 1x (Invitrogen), 0.1 mM beta-mercaptoethanol). Cells were fed daily
794 and split based on confluency. As differentiation of the G4 mESC line was slightly more robust
795 this was used routinely, and data shown refers to G4 ESC-derived neurons unless otherwise
796 stated.

797 Neural differentiation was initiated by dissociating the mESC colonies using Accutase
798 and excess feeder cells were removed from the cell suspensions by panning on gelatin-coated
799 plates. Dissociated cells were counted and transferred to ultra-low attachment cell culture
800 plates at a dilution of 220,000 cells/ml, in differentiation medium (Dulbecco's Modified Eagle
801 Medium (DMEM) (GIBCO), 10% Hyclone defined FBS (GE Healthcare), 1x L-Glutamax, 1x
802 sodium pyruvate, 1x NEAA (GIBCO), and 0.1 mM beta-mercaptoethanol). Neural induction
803 was continued for 8 days, medium was changed every two days, and supplemented with 5
804 µM retinoic acid for the final 4 days. Cell aggregates were dissociated using Accutase, single
805 cell selected through a 40 µm cell strainer, and plated onto 0.1 mg/ml poly-ornithine / 4 µg/ml
806 laminin-coated plates in N2 medium (DMEM/F12, 1x Glutamax 1x N2 supplement, 20 µg/ml
807 insulin, 50 µg/ml BSA) at a density of 50,000-100, 000 cells/cm². After 2 days, cells were
808 changed into N2B27 (Neurobasal, 1x N2 supplement, 1x B27 supplement, 1x Glutamax).
809 N2B27 was changed every 4 days for 12 days, following which 50% media changes were
810 performed for the remaining culture time.

811 High potassium-mediated depolarisation was performed as previously described
812 (Martin et al., 2014). Briefly, cells were washed with low K⁺ buffer (15 mM HEPES, 145 mM
813 NaCl, 5.6 mM KCl, 2.2 mM CaCl₂, 0.5 mM MgCl₂, 5.6 mM D-glucose, 0.5 mM ascorbic acid,
814 0.1% BSA, pH 7.4), transferred to high K⁺ buffer for 5 min (formulation as the low K⁺ buffer
815 but using 95 mM NaCl and 56 mM KCl), washed again in low K⁺ buffer and either harvested
816 directly for RNA, immediately fixed for ICC, or chased in growth medium for the appropriate
817 times prior to fixation or RNA extraction.

818

819 *Human in vitro neuron differentiation*

820 Human neurons were generated following two different approaches: either as adherent
821 monolayer cultures via a neural stem cell intermediate population (Reinhardt et al., 2013) or
822 as cerebral organoids (Lancaster and Knoblich, 2014). For adherent cultures, PSCs were
823 disaggregated mechanically and cultivated as embryoid bodies in DMEM/F12 and Neurobasal
824 1;1 mix, 1% Glutamax (all Life Technologies) with 1:200 N2 Supplement (R&D Systems),
825 1:100 B27 supplement without retinoic acid (Miltenyi Biotec) supplemented with 10 μ M SB-
826 431542, 1 μ M dorsomorphin (both Selleckchem), 3 μ M CHIR 99021 (Cayman Chemical
827 Company) and 0.5 μ M PMA (Sigma) for 3 days on petri dishes. On day 4, SB-431542 and
828 dorsomorphin were removed and 150 μ M ascorbic acid (Cayman Chemical Company) was
829 added to the media. On day 6, cells were plated onto Matrigel- (Corning) coated TC dishes to
830 allow attachment of neuroepithelial cell types. Over several passages, neural stem cells were
831 enriched resulting in pure populations. These neural stem cells could be differentiated by
832 removing the small molecules from the media and switching to B27 supplement with retinoic
833 acid, resulting in a mixed population of beta3-Tubulin positive neurons and GFAP-positive glia
834 within 4 weeks. For cerebral organoids, PSCs were dissociated into single cells and plated in
835 a ultra-low-attachment 96 well plate using 9,000 cells/ well in E8 media (Life Technologies),
836 with 50 μ M Y-27632 (Selleckchem). After 5-6 days, embryoid bodies were transferred to ultra-
837 low-attachment 6-well TC plates in neural induction media (DMEM/F12, 1% Glutamax, 1%
838 non-essential amino acids and 10 μ g/ml heparin (Sigma). After another 4-5 days, organoids
839 were embedded into Cultrex (R&D Systems) matrix and cultivated under continuous agitation
840 on an orbital shaker in cerebral organoid media (DMEM/F12 and Neurobasal 1;1 mix, 1%
841 Glutamax, 0.5% non-essential amino acids, 1:200 N2 Supplement, 1:100 B27 supplement
842 (Miltenyi Biotec) and 1:40,000 Insulin (Sigma), with media changes every 3 days until a
843 maximum age of 9 months.

844

845 *RT-qPCR*

846 Total RNA was extracted using the Macherey-Nagel NucleoSpin RNA kit, including on
847 column digestion of DNA with RNase-free DNase according to manufacturer's specifications.
848 Concentration and 260/280 ratios were quantified using a NanoDrop 1000 spectrophotometer
849 before cDNA synthesis using the iScript cDNA synthesis kit (Bio-Rad). Primers were designed
850 to span exon-exon boundaries wherever possible (Supplementary Table 2). When this was
851 not possible, samples were excluded if genomic DNA contamination was more than 10-fold
852 over the cDNA concentration. Quantitative PCR (qPCR) reactions used SsoFast Evagreen
853 (Bio-Rad) with cDNA template according to manufacturer's instructions, using a C1000
854 Thermocycler (Bio-Rad) and CFX software. Results were analysed as described previously
855 (Livak and Schmittgen, 2001).

856

857 *Immunocytochemistry*

858 Protein ICC was performed as described previously (Martin et al., 2013) on cells fixed
859 in 4% paraformaldehyde or 2% paraformaldehyde (Electron Microscopy Sciences). For double
860 and triple immunocytochemistry using antibodies to methylated DNA, an alternative sequential
861 labelling method was used. Briefly, cells were fixed in 2% PFA/PBS for 10-30 min,
862 permeabilised for 1 h in 0.5% TX-100, then depleted of residual methylated RNA using RNase
863 A at 10 µg/ml for 30 min at 37°C in PBS. Cells were subsequently blocked in PBS/0.2%
864 BSA/0.2% cold-water fish skin gelatin for 10 min, then labelled with protein-targeting
865 antibodies in PBS/0.2% BSA/0.2% cold-water fish skin gelatin overnight at 4°C. Cells were
866 then washed with PBS, labelled using corresponding secondary antibodies in PBS/0.2%
867 BSA/0.2% cold-water fish skin gelatin for 30 min, washed in PBS, then re-fixed in 2%
868 PFA/PBS for 15 min. DNA epitopes were retrieved using 4N HCl/0.1% TX-100 for 10 min at

869 room temp, cells washed in PBS/0.05% Tween-20, and blocked in PBS/0.05% Tween-20/1%
870 BSA (BS) for 1 h. Antibodies to methylated DNA were applied in PBS/0.05% Tween-20/1%
871 BSA overnight at 4°C. Cells were subsequently washed in PBS/0.05% Tween-20/1% BSA and
872 appropriate secondary antibodies applied in the same buffer containing 0.1 µg/ml DAPI for 30
873 min-1 h. Finally, cells were washed in PBS/0.05% Tween-20/1% BSA, rinsed in PBS and
874 either imaged directly (high throughput imaging), or mounted in Mowiol (Confocal).

875

876 *Immunohistochemistry*

877 Mouse brain sections were fixed in 2% PFA for 30 min, then permeabilised in
878 PBS/0.5% Triton X-100 for 1h, blocked in BS for 1h and incubated overnight at 4°C with a
879 NeuN antibody (1:2500) in BS. They were subsequently incubated for 1h with a secondary
880 fluorescently labelled antibody in BS (1:1000). After post-fixation with 2% PFA for 10 min, to
881 obtain access to DNA methyl groups, cell nuclei were mildly depurinated with 4N HCl treatment
882 for 15 min and incubated with antibody-enriched culture medium against mCG or mCA in BS
883 overnight at 4°C. After incubation for 1h with a secondary fluorescently labelled antibody in
884 BS (1:1000) the tissue was stained with 1:100 YOYO1 (Molecular Probes, Life Technologies)
885 for 15 min and mounted with Vectashield Antifade Mounting Medium (H-1000, Vector
886 Laboratories). Washing with PBS/0.05% Tween-20 for 1-2h was performed after each step,
887 reagents were dissolved in PBS/0.05% Tween-20 and steps performed at room temperature,
888 unless otherwise stated.

889

890 *Microscopy*

891 Phase contrast microscopy was performed on live cells using an Olympus IX51.
892 Confocal microscopy was performed on fixed cells using either a Zeiss 710 confocal
893 microscope and a 40x water immersion objective or a Leica SP8 confocal microscope using

894 a 60x oil immersion objective. High throughput imaging was performed using a Perkin-Elmer
895 Operetta equipped with a 20x Air objective. Brain section imaging was performed with Nikon
896 A1-R confocal microscope and a 60x 1.4 NA oil immersion objective.

897 Image analysis was performed by manual masking of nuclei and measuring
898 fluorescence intensity/nucleus using Image J (Figure 1J, L) or by high-throughput Operetta
899 image acquisition using Harmony (Figure 1D, F, H; Supplementary Figure 1E; Supplementary
900 Figure 2B), prior to exporting the images, generating nuclear masks and analysing
901 fluorescence intensity using Cell Profiler (Carpenter et al., 2006). All image analysis data was
902 collated using Excel 2016, and graphs prepared using Excel for Office 365 or Graphpad Prism
903 8. All images were processed using Adobe Photoshop 2020 and figures compiled with Adobe
904 Illustrator 2020.

905

906 *Transmission electron microscopy*

907 ESC-derived neurons were incubated with 10 µg/ml CTB-HRP in either high K⁺ or low
908 K⁺ buffer for 5 min, washed in PBS and fixed in 2.5% glutaraldehyde (Electron Microscopy
909 Sciences) for 24 h. Following fixation, cells were processed for 3, 39-diaminobenzidine (DAB)
910 cytochemistry using standard protocols. Fixed cells were contrasted with 1% osmium tetroxide
911 and 4% uranyl acetate prior to dehydration and embedding in LX-112 resin (Martin et al.,
912 2013). Sections (~50 nm) were cut using an ultramicrotome (UC64; Leica). To determine CTB-
913 HRP endocytosis, presynaptic regions were visualized at 60,000x using a transmission
914 electron microscope (model 1011; JEOL) equipped with a Morada cooled CCD camera and
915 the iTEM AnalySIS software.

916

917 *Whole genome bisulfite sequencing*

918 DNA methylation analysis by WGBS was performed using approximately 100,000 cells.
919 Genomic DNA was isolated with the DNeasy Blood and Tissue Kit (Qiagen) with some
920 modifications: samples were incubated for 4 h at 56°C with an additional RNase A incubation
921 for 30 min at 37°C. 500 ng of genomic DNA spiked with 4% (w/w) unmethylated lambda phage
922 DNA (Thermo Fisher Scientific) was sheared to a mean length of 200 bp using the Covaris
923 S220 focused-ultrasonicator. Libraries for WGBS were prepared as follows: DNA fragments
924 were end-repaired using the End-It kit (Epicentre), A-tailed with Klenow exo- (NEB) and ligated
925 to methylated Illumina TruSeq adapters (BIOO Scientific) with DNA Ligase (NEB), followed by
926 bisulfite conversion using EZ DNA-methylation Gold kit (Zymo Research). Library fragments
927 were then subjected to 7 cycles of PCR amplification with KAPA HiFi Uracil+ DNA polymerase
928 (KAPA Biosystems). Single-end 100 bp sequencing was performed on a HiSeq 1500 or a
929 MiSeq (Illumina).

930

931 *DNA methylation analysis*

932 Reads were trimmed for quality and adapter sequences removed. Following pre-processing,
933 reads were aligned to mm10 or hg19 references with Bowtie and a pipeline described
934 previously (Langmead et al., 2009, Lister et al., 2009), resulting in a table summarising
935 methylated and unmethylated read counts for each covered cytosine position in the genome.
936 Bisulfite non-conversion frequency was calculated as the percentage of cytosine base calls at
937 reference cytosine positions in the unmethylated lambda control genome. This was performed
938 individually for each context (CA, CC, CG, CT). Methylation for particular genomic contexts
939 and average methylation of gene bodies were calculated by intersecting whole genome data
940 with feature bed files from the UCSC table browser using Bedtools (Quinlan, 2014). For
941 correlation, heatmap generation and clustering of methylation data, Deeptools was used
942 (Ramirez et al., 2016), along with R using packages pals, gplots, ggplot2, viridis and
943 RColorBrewer. When calculating average methylation level in a region (weighted methylation

944 level), the number of C basecalls divided by total sequence coverage at reference C positions
945 was used to calculate the methylation level for each context (CG, CH, CA, CC, CT). Sample-
946 specific and context-specific bisulfite non-conversion rates, calculated from the unmethylated
947 lambda phage DNA control, were subtracted for each methylation context. Gene set
948 enrichment analysis was performed using the fgsea package for R (Subramanian et al., 2005)
949 with reactome (Fabregat et al., 2018) and gene ontology annotations (Ashburner et al., 2000,
950 The Gene Ontology, 2019). Pathways were sorted by NES score (enrichment score
951 normalized to mean enrichment of random samples of the same size) and only pathways with
952 p-value < 0.05 were considered in subsequent analyses.

953 For similarity analysis, every gene was given a score as follows: First, the difference
954 in weighted DNA methylation between *in vivo* and *in vitro* neurons (y) was calculated for each
955 gene and scaled to a value between 0 and 1 (using the formula $x = |y-1|$), so that genes that
956 were more similar in methylation state between both samples would have a value (x) closer to
957 1. Then, the average of weighted DNA methylation per gene in neuronal samples was
958 compared against the average weighted DNA methylation of glial and fetal samples, resulting
959 again in a score between 0 and 1, with genes showing greater differences having a value
960 closer to 1. Both scores for similarity between neurons and dissimilarity to non-neuronal
961 samples were added in order to give both aspects the same weight, and scaled to values
962 between 0 and 1, with values closer to 1 representing genes being more similar in methylation
963 state between both neuronal samples but different compared to glia and fetal frontal cortex.
964 This similarity score was then used to rank all genes for GSEA using the fgsea package as
965 described above.

966

967 *Fluorescence-activated nuclear sorting*

968 Intact nuclei were isolated from cell pellets as described previously (Li et al., 2014,
969 Okada et al., 2011). Briefly, cells were Dounce-homogenised on ice in chilled nuclear

970 extraction buffer (10 mM Tris-HCl, pH 8, 0.32 M sucrose, 5 mM CaCl₂, 3 mM Mg(Ac)₂, 0.1 mM
971 EDTA, 1 mM DTT, 1x protease inhibitor cocktail (Merck), 0.3% Triton X-100). Nuclear lysates
972 were filtered (40 µm), centrifuged for 7 min at 3000 rpm at 4°C and resuspended in PBS.
973 Nuclei were blocked with 10% normal goat serum and labelled for 60 min on ice with either
974 directly conjugated mouse anti-NeuN-Alexa488, or pre-conjugated rabbit anti-Nanog/goat
975 anti-rabbit Alexa488 or rabbit anti-Pax6/goat anti-rabbit Alexa488 complexes. Samples of
976 each nuclear fraction were retained for secondary only antibody controls. 7-AAD (20 µg/ml)
977 was added all samples 15 min prior to sorting. A BD Influx cell sorter was used to sort nuclei.
978 Prior to sorting, the secondary only control was used to gate events to isolate nuclei from cell
979 debris. From the selected nuclear populations, nuclei were separated into distinct NeuN+ve/7-
980 AAD+ve and NeuN-ve/7-AAD+ve populations, Nanog+ve/7-AAD+ve and Pax6+ve/7-AAD+ve
981 populations, depending upon the cell type.

982

983 *Statistical Analysis*

984 All data was analysed using an unpaired, two-tailed Student's t-test, unless stated otherwise.

985

986 **Acknowledgements**

987 Funding: Monoclonal antibody generation and N.O. were funded by the Babraham Institute
988 Knowledge Exchange and Commercialisation Fund, W.R. is funded by the BBSRC. E.W. was
989 funded by NHMRC APP1130168 and NHMRC APP1090116 project grants. R.L. was
990 supported by a Sylvia and Charles Viertel Senior Medical Research Fellowship and Howard
991 Hughes Medical Institute International Research Scholarship, and research activities by
992 NHMRC GNT1130168 and GNT1090116 Project Grants.

993

994 Methylated oligonucleotide sequences were kindly provided by Dr Akanksha Singh, Active
995 Motif (Carlsbad, CA). KLH-conjugated dinucleotides for monoclonal antibody generation were
996 kindly provided by Active Motif Inc. The R1 and G4 mESC cell lines were provided by Prof
997 Peter Koopman (IMB, UQ) and Dr Josephine Bowles (SBMS, UQ). Electron microscopy was
998 performed at the Australian Microscopy and Microanalysis Facility at the Centre for
999 Microscopy and Microanalysis at the University of Queensland. Confocal microscopy (apart
1000 from Nikon A1-R) was performed at the Queensland node of the Australian National
1001 Fabrication Facility, a company established under the National Collaborative Research
1002 Infrastructure Strategy to provide nano- and micro-fabrication facilities for Australia's
1003 researchers. Fluorescent-activated nuclear sorting was performed by the Queensland Brain
1004 Institute Flow Cytometry Facility. We thank Lidia Madrid and Zukrofi Muzar for expert technical
1005 assistance and Gavin Kelsey (Babraham Institute, UK) for providing reagents. We thank
1006 Saskia Freytag for her assistance with R scripting. We thank Marga Behrens for insightful
1007 discussions on DNA methylation dynamics during brain development.

1008

1009 **Data availability**

1010 WGBS data is available in GEO under the accession number GSE137098.

1011

1012

1013

1014

1015 **Table 1 Antibodies**

1016

Target	Host	Clone	Supplier	Catalog #
TUBB3 (Beta III Tubulin)	Rabbit		Sigma-Aldrich	T2200
TUBB3 (Beta III Tubulin)	Chicken		Merck-Millipore	AB9354
NeuN (ICC)	Rabbit	D4G4O	Cell Signaling Technology	24307
NeuN (IHC)	Rabbit		Abcam	ab128886
NeuN-Alexa488	Mouse	A60	Merck-Millipore	MAB377X
c-Fos	Guinea pig		Synaptic Systems	226 004
Synapsin 1	Rabbit		Merck-Millipore	AB154
Pax6	Rabbit	Poly19013	BioLegend	19013
5-mC	Rabbit	RM231	Abcam	ab214727
5-hmC	Rabbit		Active Motif	39769
mCA	Mouse	2C8H8A6	Available through Active Motif	61783/4
mCG	Mouse	3A7	Reik Laboratory, Babraham Institute	-
GFAP	Rabbit		Dako	Z0344
Nanog	Rabbit	D2A3	Cell Signaling Technology	8822

1017

1018

1019 **Table 2 RT-qPCR primers**

1020

Target	Gene ID	Forward primer	Reverse Primer	Ref.
beta-Actin	11461	AAGATCAAGATCATTGCTCCTCT	CAGCTCAGTAACAGTCCGCC	-
NeuN/RbFox3	52897	ATCGTAGAGGGACGGAAAATTGA	GTTCCCAGGCTTCTTATTGGTC	-
Dnmt1	13433	AAGAATGGTGTTGTCTACCGAC	CATCCAGGTTGCTCCCCTTG	<i>(Zeisel et al., 2013)</i>
Dnmt3a	13435	GATGAGCCTGAGTATGAGGATGG	CAAGACACAATTCGGCCTGG	-
c-Fos	14281	CCTACTACCATTCCCCAGCC	CTGTCACCGTGGGGATAAAG	<i>(Mikuni et al., 2013)</i>

1021

1022

1023

1024 References

- 1025 Arand, J., Spieler, D., Karius, T., *et al.* 2012. In vivo control of CpG and non-CpG DNA
1026 methylation by DNA methyltransferases. *PLoS Genet*, 8, e1002750.
- 1027 Ashburner, M., Ball, C. A., Blake, J. A., *et al.* 2000. Gene ontology: tool for the unification of
1028 biology. The Gene Ontology Consortium. *Nat Genet*, 25, 25-9.
- 1029 Bayraktar, G. & Kreutz, M. R. 2018a. Neuronal DNA Methyltransferases: Epigenetic Mediators
1030 between Synaptic Activity and Gene Expression? *Neuroscientist*, 24, 171-185.
- 1031 Bayraktar, G. & Kreutz, M. R. 2018b. The Role of Activity-Dependent DNA Demethylation in
1032 the Adult Brain and in Neurological Disorders. *Front Mol Neurosci*, 11, 169.
- 1033 Benito-Kwiecinski, S. & Lancaster, M. A. 2019. Brain Organoids: Human Neurodevelopment
1034 in a Dish. *Cold Spring Harb Perspect Biol*.
- 1035 Bibel, M., Richter, J., Lacroix, E., *et al.* 2007. Generation of a defined and uniform population
1036 of CNS progenitors and neurons from mouse embryonic stem cells. *Nat Protoc*, 2,
1037 1034-43.
- 1038 Bibel, M., Richter, J., Schrenk, K., *et al.* 2004. Differentiation of mouse embryonic stem cells
1039 into a defined neuronal lineage. *Nat Neurosci*, 7, 1003-9.
- 1040 Bird, A. 2002. DNA methylation patterns and epigenetic memory. *Genes Dev*, 16, 6-21.
- 1041 Cakir, B., Xiang, Y., Tanaka, Y., *et al.* 2019. Engineering of human brain organoids with a
1042 functional vascular-like system. *Nat Methods*, 16, 1169-1175.
- 1043 Carpenter, A. E., Jones, T. R., Lamprecht, M. R., *et al.* 2006. CellProfiler: image analysis
1044 software for identifying and quantifying cell phenotypes. *Genome Biol*, 7, R100.
- 1045 Chahrour, M. & Zoghbi, H. Y. 2007. The story of Rett syndrome: from clinic to neurobiology.
1046 *Neuron*, 56, 422-37.
- 1047 Chen, L., Chen, K., Lavery, L. A., *et al.* 2015. MeCP2 binds to non-CG methylated DNA as
1048 neurons mature, influencing transcription and the timing of onset for Rett syndrome.
1049 *Proc Natl Acad Sci U S A*, 112, 5509-14.
- 1050 Chen, Y., Damayanti, N. P., Irudayaraj, J., *et al.* 2014. Diversity of two forms of DNA
1051 methylation in the brain. *Front Genet*, 5, 46.
- 1052 Cortes-Mendoza, J., Diaz De Leon-Guerrero, S., Pedraza-Alva, G., *et al.* 2013. Shaping
1053 synaptic plasticity: the role of activity-mediated epigenetic regulation on gene
1054 transcription. *Int J Dev Neurosci*, 31, 359-69.
- 1055 Cousin, M. A. 2009. Activity-dependent bulk synaptic vesicle endocytosis--a fast, high capacity
1056 membrane retrieval mechanism. *Mol Neurobiol*, 39, 185-9.
- 1057 Day, J. J., Childs, D., Guzman-Karlsson, M. C., *et al.* 2013. DNA methylation regulates
1058 associative reward learning. *Nat Neurosci*, 16, 1445-52.
- 1059 Fabregat, A., Jupe, S., Matthews, L., *et al.* 2018. The Reactome Pathway Knowledgebase.
1060 *Nucleic Acids Res*, 46, D649-D655.
- 1061 Fasolino, M. & Zhou, Z. 2017. The Crucial Role of DNA Methylation and MeCP2 in Neuronal
1062 Function. *Genes (Basel)*, 8.
- 1063 Feng, J., Chang, H., Li, E., *et al.* 2005. Dynamic expression of de novo DNA
1064 methyltransferases Dnmt3a and Dnmt3b in the central nervous system. *J Neurosci*
1065 *Res*, 79, 734-46.
- 1066 Feng, J. & Fan, G. 2009. The role of DNA methylation in the central nervous system and
1067 neuropsychiatric disorders. *Int Rev Neurobiol*, 89, 67-84.
- 1068 Feng, J., Zhou, Y., Campbell, S. L., *et al.* 2010. Dnmt1 and Dnmt3a maintain DNA methylation
1069 and regulate synaptic function in adult forebrain neurons. *Nat Neurosci*, 13, 423-30.
- 1070 Fraser, J., Ferrai, C., Chiariello, A. M., *et al.* 2015. Hierarchical folding and reorganization of
1071 chromosomes are linked to transcriptional changes in cellular differentiation. *Mol Syst*
1072 *Biol*, 11, 852.
- 1073 Furlanis, E. & Scheiffele, P. 2018. Regulation of Neuronal Differentiation, Function, and
1074 Plasticity by Alternative Splicing. *Annu Rev Cell Dev Biol*, 34, 451-469.
- 1075 Gabel, H. W., Kinde, B., Stroud, H., *et al.* 2015. Disruption of DNA-methylation-dependent
1076 long gene repression in Rett syndrome. *Nature*, 522, 89-93.

- 1077 Gallegos, D. A., Chan, U., Chen, L. F., *et al.* 2018. Chromatin Regulation of Neuronal
1078 Maturation and Plasticity. *Trends Neurosci*, 41, 311-324.
- 1079 George, S. H., Gertsenstein, M., Vintersten, K., *et al.* 2007. Developmental and adult
1080 phenotyping directly from mutant embryonic stem cells. *Proc Natl Acad Sci U S A*, 104,
1081 4455-60.
- 1082 Graff, J., Woldemichael, B. T., Berchtold, D., *et al.* 2012. Dynamic histone marks in the
1083 hippocampus and cortex facilitate memory consolidation. *Nat Commun*, 3, 991.
- 1084 Guarda, A., Bolognese, F., Bonapace, I. M., *et al.* 2009. Interaction between the inner nuclear
1085 membrane lamin B receptor and the heterochromatic methyl binding protein, MeCP2.
1086 *Exp Cell Res*, 315, 1895-903.
- 1087 Guo, J. U., Su, Y., Shin, J. H., *et al.* 2014. Distribution, recognition and regulation of non-CpG
1088 methylation in the adult mammalian brain. *Nat Neurosci*, 17, 215-22.
- 1089 Hamidi, T., Singh, A. K. & Chen, T. 2015. Genetic alterations of DNA methylation machinery
1090 in human diseases. *Epigenomics*, 7, 247-65.
- 1091 He, Y. & Ecker, J. R. 2015. Non-CG Methylation in the Human Genome. *Annu Rev Genomics*
1092 *Hum Genet*, 16, 55-77.
- 1093 Hubbard, K. S., Gut, I. M., Lyman, M. E., *et al.* 2013. Longitudinal RNA sequencing of the
1094 deep transcriptome during neurogenesis of cortical glutamatergic neurons from murine
1095 ESCs. *F1000Res*, 2, 35.
- 1096 Ip, J. P. K., Mellios, N. & Sur, M. 2018. Rett syndrome: insights into genetic, molecular and
1097 circuit mechanisms. *Nat Rev Neurosci*, 19, 368-382.
- 1098 Kang, H. J., Kawasawa, Y. I., Cheng, F., *et al.* 2011. Spatio-temporal transcriptome of the
1099 human brain. *Nature*, 478, 483-9.
- 1100 Kinde, B., Wu, D. Y., Greenberg, M. E., *et al.* 2016. DNA methylation in the gene body
1101 influences MeCP2-mediated gene repression. *Proc Natl Acad Sci U S A*, 113, 15114-
1102 15119.
- 1103 Kishi, N. & Macklis, J. D. 2004. MECP2 is progressively expressed in post-migratory neurons
1104 and is involved in neuronal maturation rather than cell fate decisions. *Mol Cell*
1105 *Neurosci*, 27, 306-21.
- 1106 Kriaucionis, S. & Heintz, N. 2009. The nuclear DNA base 5-hydroxymethylcytosine is present
1107 in Purkinje neurons and the brain. *Science*, 324, 929-30.
- 1108 Lager, S., Connelly, J. C., Schweikert, G., *et al.* 2017. MeCP2 recognizes cytosine
1109 methylated tri-nucleotide and di-nucleotide sequences to tune transcription in the
1110 mammalian brain. *PLoS Genet*, 13, e1006793.
- 1111 Lancaster, M. A. & Knoblich, J. A. 2014. Generation of cerebral organoids from human
1112 pluripotent stem cells. *Nat Protoc*, 9, 2329-40.
- 1113 Langmead, B., Trapnell, C., Pop, M., *et al.* 2009. Ultrafast and memory-efficient alignment of
1114 short DNA sequences to the human genome. *Genome Biol*, 10, R25.
- 1115 Lanoue, V., Langford, M., White, A., *et al.* 2017. The Wnt receptor Ryk is a negative regulator
1116 of mammalian dendrite morphogenesis. *Sci Rep*, 7, 5965.
- 1117 Li, X., Baker-Andresen, D., Zhao, Q., *et al.* 2014. Methyl CpG binding domain ultra-
1118 sequencing: a novel method for identifying inter-individual and cell-type-specific
1119 variation in DNA methylation. *Genes Brain Behav*, 13, 721-31.
- 1120 Liao, J., Karnik, R., Gu, H., *et al.* 2015. Targeted disruption of DNMT1, DNMT3A and DNMT3B
1121 in human embryonic stem cells. *Nat Genet*, 47, 469-78.
- 1122 Lister, R., Mukamel, E. A., Nery, J. R., *et al.* 2013. Global epigenomic reconfiguration during
1123 mammalian brain development. *Science*, 341, 1237905.
- 1124 Lister, R., Pelizzola, M., Dowen, R. H., *et al.* 2009. Human DNA methylomes at base resolution
1125 show widespread epigenomic differences. *Nature*, 462, 315-22.
- 1126 Livak, K. J. & Schmittgen, T. D. 2001. Analysis of relative gene expression data using real-
1127 time quantitative PCR and the 2^{(-Delta Delta C(T))} Method. *Methods*, 25, 402-8.
- 1128 Luo, C., Keown, C. L., Kurihara, L., *et al.* 2017. Single-cell methylomes identify neuronal
1129 subtypes and regulatory elements in mammalian cortex. *Science*, 357, 600-604.
- 1130 Luo, C., Lee, Q. Y., Wapinski, O., *et al.* 2019. Global DNA methylation remodeling during direct
1131 reprogramming of fibroblasts to neurons. *Elife*, 8.

- 1132 Mansour, A. A., Goncalves, J. T., Bloyd, C. W., *et al.* 2018. An in vivo model of functional and
1133 vascularized human brain organoids. *Nat Biotechnol*, 36, 432-441.
- 1134 Martin, S., Papadopulos, A., Tomatis, V. M., *et al.* 2014. Increased polyubiquitination and
1135 proteasomal degradation of a Munc18-1 disease-linked mutant causes temperature-
1136 sensitive defect in exocytosis. *Cell Rep*, 9, 206-18.
- 1137 Martin, S., Tomatis, V. M., Papadopulos, A., *et al.* 2013. The Munc18-1 domain 3a loop is
1138 essential for neuroexocytosis but not for syntaxin-1A transport to the plasma
1139 membrane. *J Cell Sci*, 126, 2353-60.
- 1140 Maunakea, A. K., Chepelev, I., Cui, K., *et al.* 2013. Intragenic DNA methylation modulates
1141 alternative splicing by recruiting MeCP2 to promote exon recognition. *Cell Res*, 23,
1142 1256-69.
- 1143 Mellen, M., Ayata, P., Dewell, S., *et al.* 2012. MeCP2 binds to 5hmC enriched within active
1144 genes and accessible chromatin in the nervous system. *Cell*, 151, 1417-30.
- 1145 Mikuni, T., Uesaka, N., Okuno, H., *et al.* 2013. Arc/Arg3.1 is a postsynaptic mediator of activity-
1146 dependent synapse elimination in the developing cerebellum. *Neuron*, 78, 1024-35.
- 1147 Miller, C. A. & Sweatt, J. D. 2007. Covalent modification of DNA regulates memory formation.
1148 *Neuron*, 53, 857-69.
- 1149 Mo, A., Mukamel, E. A., Davis, F. P., *et al.* 2015. Epigenomic Signatures of Neuronal Diversity
1150 in the Mammalian Brain. *Neuron*, 86, 1369-84.
- 1151 Mullen, R. J., Buck, C. R. & Smith, A. M. 1992. NeuN, a neuronal specific nuclear protein in
1152 vertebrates. *Development*, 116, 201-11.
- 1153 Nagy, A., Rossant, J., Nagy, R., *et al.* 1993. Derivation of completely cell culture-derived mice
1154 from early-passage embryonic stem cells. *Proc Natl Acad Sci U S A*, 90, 8424-8.
- 1155 Nguyen, S., Meletis, K., Fu, D., *et al.* 2007. Ablation of de novo DNA methyltransferase
1156 Dnmt3a in the nervous system leads to neuromuscular defects and shortened lifespan.
1157 *Dev Dyn*, 236, 1663-76.
- 1158 Okada, S., Saiwai, H., Kumamaru, H., *et al.* 2011. Flow cytometric sorting of neuronal and
1159 glial nuclei from central nervous system tissue. *J Cell Physiol*, 226, 552-8.
- 1160 Peric-Hupkes, D., Meuleman, W., Pagie, L., *et al.* 2010. Molecular maps of the reorganization
1161 of genome-nuclear lamina interactions during differentiation. *Mol Cell*, 38, 603-13.
- 1162 Quinlan, A. R. 2014. BEDTools: The Swiss-Army Tool for Genome Feature Analysis. *Curr*
1163 *Protoc Bioinformatics*, 47, 11 12 1-34.
- 1164 Ramirez, F., Ryan, D. P., Gruning, B., *et al.* 2016. deepTools2: a next generation web server
1165 for deep-sequencing data analysis. *Nucleic Acids Res*, 44, W160-5.
- 1166 Ramsahoye, B. H., Biniszkiwicz, D., Lyko, F., *et al.* 2000. Non-CpG methylation is prevalent
1167 in embryonic stem cells and may be mediated by DNA methyltransferase 3a. *Proc Natl*
1168 *Acad Sci U S A*, 97, 5237-42.
- 1169 Reinhardt, P., Glatza, M., Hemmer, K., *et al.* 2013. Derivation and expansion using only small
1170 molecules of human neural progenitors for neurodegenerative disease modeling.
1171 *PLoS One*, 8, e59252.
- 1172 Schubeler, D. 2015. Function and information content of DNA methylation. *Nature*, 517, 321-
1173 6.
- 1174 Skene, P. J., Illingworth, R. S., Webb, S., *et al.* 2010. Neuronal MeCP2 is expressed at near
1175 histone-octamer levels and globally alters the chromatin state. *Mol Cell*, 37, 457-68.
- 1176 Stiles, J. & Jernigan, T. L. 2010. The basics of brain development. *Neuropsychol Rev*, 20,
1177 327-48.
- 1178 Stroud, H., Su, S. C., Hrvatin, S., *et al.* 2017. Early-Life Gene Expression in Neurons
1179 Modulates Lasting Epigenetic States. *Cell*, 171, 1151-1164 e16.
- 1180 Subramanian, A., Tamayo, P., Mootha, V. K., *et al.* 2005. Gene set enrichment analysis: a
1181 knowledge-based approach for interpreting genome-wide expression profiles. *Proc*
1182 *Natl Acad Sci U S A*, 102, 15545-50.
- 1183 Szulwach, K. E., Li, X., Li, Y., *et al.* 2011. 5-hmC-mediated epigenetic dynamics during
1184 postnatal neurodevelopment and aging. *Nat Neurosci*, 14, 1607-16.

- 1185 Tan, H. K., Wu, C. S., Li, J., *et al.* 2019. DNMT3B shapes the mCA landscape and regulates
1186 mCG for promoter bivalency in human embryonic stem cells. *Nucleic Acids Res*, 47,
1187 7460-7475.
- 1188 The Gene Ontology, C. 2019. The Gene Ontology Resource: 20 years and still GOing strong.
1189 *Nucleic Acids Res*, 47, D330-D338.
- 1190 Walczak, A., Szczepankiewicz, A. A., Ruszczycki, B., *et al.* 2013. Novel higher-order
1191 epigenetic regulation of the Bdnf gene upon seizures. *J Neurosci*, 33, 2507-11.
- 1192 Weyn-Vanhenenryck, S. M., Feng, H., Ustianenko, D., *et al.* 2018. Precise temporal
1193 regulation of alternative splicing during neural development. *Nat Commun*, 9, 2189.
- 1194 Williams, R. R., Azuara, V., Perry, P., *et al.* 2006. Neural induction promotes large-scale
1195 chromatin reorganisation of the Mash1 locus. *J Cell Sci*, 119, 132-40.
- 1196 Wu, X. & Zhang, Y. 2017. TET-mediated active DNA demethylation: mechanism, function and
1197 beyond. *Nat Rev Genet*, 18, 517-534.
- 1198 Xie, W., Barr, C. L., Kim, A., *et al.* 2012. Base-resolution analyses of sequence and parent-of-
1199 origin dependent DNA methylation in the mouse genome. *Cell*, 148, 816-31.
- 1200 Yazdani, M., Deogracias, R., Guy, J., *et al.* 2012. Disease modeling using embryonic stem
1201 cells: MeCP2 regulates nuclear size and RNA synthesis in neurons. *Stem Cells*, 30,
1202 2128-39.
- 1203 Young, J. I., Hong, E. P., Castle, J. C., *et al.* 2005. Regulation of RNA splicing by the
1204 methylation-dependent transcriptional repressor methyl-CpG binding protein 2. *Proc*
1205 *Natl Acad Sci U S A*, 102, 17551-8.
- 1206 Zeisel, A., Yitzhaky, A., Bossel Ben-Moshe, N., *et al.* 2013. An accessible database for mouse
1207 and human whole transcriptome qPCR primers. *Bioinformatics*, 29, 1355-6.
- 1208 Ziller, M. J., Muller, F., Liao, J., *et al.* 2011. Genomic distribution and inter-sample variation of
1209 non-CpG methylation across human cell types. *PLoS Genet*, 7, e1002389.
- 1210 Zuleger, N., Robson, M. I. & Schirmer, E. C. 2011. The nuclear envelope as a chromatin
1211 organizer. *Nucleus*, 2, 339-49.
- 1212